

# BRNO UNIVERSITY OF TECHNOLOGY

VYSOKÉ UČENÍ TECHNICKÉ V BRNĚ

## FACULTY OF MECHANICAL ENGINEERING

FAKULTA STROJNÍHO INŽENÝRSTVÍ

## INSTITUTE OF PHYSICAL ENGINEERING

ÚSTAV FYZIKÁLNÍHO INŽENÝRSTVÍ

# SELF-ASSEMBLED MOLECULAR LAYERS ON EPITAXIAL GRAPHENE

SAMOUSPOŘÁDANÉ MOLEKULÁRNÍ VRSTVY NA POVRCHU EPITAXNÍHO GRAFENU

## MASTER'S THESIS

DIPLOMOVÁ PRÁCE

### AUTHOR

AUTOR PRÁCE

Bc. Štěpán Kovařík

### SUPERVISOR

VEDOUcí PRÁCE

doc. Ing. Jan Čechal, Ph.D.

BRNO 2018



## **Abstract**

Molecular self-assembly is a spontaneous process of structure formation driven by intermolecular and substrate-molecule interactions. Understanding the principle of the involved processes is a key for the preparation of functional nanostructures with atomic precision. The thesis is focused on the preparation and study of the self-assembled molecular structures of 4,4'-biphenyl dicarboxylic acid on the graphene covered Ir(111) substrate. Scanning tunneling microscopy and low energy electron microscopy are employed to study molecular structure on various scales ranging from sub-nanometer to millimeter. The thesis describes a resulting molecular structure that is stable at room temperature. The assembly exhibits a binding motif determined by the interaction of two carboxyl groups.

## **Abstrakt**

Samouspořádání organických molekul je spontánní proces tvorby nanostruktur, při kterém je výsledná struktura určena mezimolekulárními a molekulárně-substrátovými interakcemi. Pochopení principů samouspořádávání je klíčem k přípravě funkčních nanostruktur s atomární přesností. Tato diplomová práce se zaměřuje na přípravu a studium samouspořádaných molekulárních struktur 4,4'-diphenyl dikarboxylové kyseliny na povrchu grafenu připraveného na Ir(111). Pro studium vlastností molekulárních struktur je využito rastrovací tunelovací mikroskopie a nízkoenergiové elektronové mikroskopie. Tato kombinace umožňuje získat informace z oblastí o velikosti v řádu nanometrů až milimetrů. V práci je popsána molekulární struktura stabilní při pokojové teplotě. Vazebný motiv této struktury je dán interakcí karboxylových skupin sousedních molekul.

## **Keywords**

Molecular self-assembly, graphene, iridium, dicarboxylic acid, STM, LEEM, XPS.

## **Klíčová slova**

Molekulární samouspořádání, grafen, iridium, dikarboxylová kyselina, STM, LEEM, XPS.

KOVAŘÍK, Š. *Self-assembled molecular layers on epitaxial graphene*. Brno: Brno University of Technology, Faculty of Mechanical Engineering, 2018. 54 s. Supervised by doc. Ing. Jan Čechal, Ph.D.



I hereby declare that I have written my master's thesis on the theme of *Self-assembled molecular layers on epitaxial graphene*, under the guidance of the master's thesis supervisor, doc. Ing. Jan Čechal, Ph.D, and using the technical literature and other sources of information which are all properly quoted in the thesis and detailed in the list of literature at the end of the thesis.

Bc. Štěpán Kovařík



My thanks go to doc. Ing. **Jan Čechal**, Ph.D., for his skillful guidance and proof-reading of the thesis. Than I would like to express my gratitude to my colleagues at CEITEC, namely: Ing. **Lukáš Kormoš**, for his introduction into the the secrets of the UHV cluster and for all assistance during experiments, Ing. **Pavel Procházka**, Ph.D., for his help with LEEM measurements and data analysis and Ing. **Anton Olegovich Makoveev**, for numerous fruitful discussions.

My deepest thanks go to Bc. **Viola Křížáková**, for everything.

Bc. Štěpán Kovařík

Financial support from the Thermo Fisher Scientific is gratefully acknowledged.

Part of the work was carried out with the support of CEITEC Nano Research Infrastructure (ID LM2015041, MEYS CR, 2016–2019), CEITEC Brno University of Technology.



# Contents

<b>Introduction</b>	<b>2</b>
<b>1 Molecular self-assembly on graphene substrate</b>	<b>4</b>
1.1 Molecular self-assembly on surfaces . . . . .	4
1.1.1 Molecular interactions . . . . .	5
1.1.2 Kinetics and thermodynamics of self-assembly process . . . . .	7
1.2 Graphene . . . . .	8
1.2.1 Graphene structure . . . . .	8
1.2.2 Graphene on various substrates . . . . .	9
1.2.3 Top-Down methods of graphene fabrication . . . . .	9
1.2.4 Bottom-up methods of graphene fabrication . . . . .	10
1.2.5 Graphene on iridium . . . . .	12
1.3 Graphene as a substrate for molecular self-assembly . . . . .	14
1.3.1 Molecular self-assembly on graphene on insulating substrate . . . . .	14
1.3.2 Graphene moiré and molecular superstructure . . . . .	15
<b>2 Experimental methods</b>	<b>16</b>
2.1 The ultra-high vacum apparatus . . . . .	16
2.2 Scanning tunneling microscopy . . . . .	18
2.2.1 Quantum tunneling effect . . . . .	19
2.2.2 Instrument . . . . .	20
2.3 Low energy electron microscopy . . . . .	21
2.3.1 LEEM instrument . . . . .	21
2.3.2 Imaging modes of LEEM . . . . .	23
2.4 Photoelectron spectroscopy . . . . .	23
<b>3 Self-assembly on graphene</b>	<b>25</b>
3.1 Biphenyl-4,4-dicarboxylic acid . . . . .	25
3.2 Preparation of the substrate for graphene growth . . . . .	26
3.2.1 STM analysis of Ir(111) surface . . . . .	28
3.3 Growth of epitaxial graphene . . . . .	29
3.3.1 STM analysis of graphene/Ir(111) . . . . .	30
3.3.2 LEEM analysis of graphene/Ir(111) . . . . .	32
3.4 Structure of self-assembled BDA layers . . . . .	33
3.4.1 STM study of BDA supramolecular structure . . . . .	34
3.4.2 LEEM study of BDA supramolecular structure . . . . .	37
3.5 Iron-coordinated BDA network . . . . .	38
3.5.1 Temperature dependent XPS study of Fe-BDA structure . . . . .	39
3.5.2 LEEM study of Fe-BDA structure . . . . .	44
<b>4 Conclusion</b>	<b>46</b>
<b>References</b>	<b>49</b>
<b>List of abbreviations</b>	<b>54</b>

# Introduction

Self-assembly is the spontaneous organization of components into patterns or structures [1]. It is a ubiquitous phenomenon, as the components may be various in nature from single atoms ordered into a crystal to whole planets assembled into galaxies. It is both a fascinating natural phenomenon of emergence of order from disorder and a powerful tool for preparation of functional structure preparation.

The driving force of the assembling process are the interactions between the components. Therefore, the resulting structure can be designed to exhibit specific properties by proper selection of the components. Organic molecules are one of the common components as they offer a virtually limitless variety of structural and functional properties. The molecular self-assembly is a prospective bottom-up technique of functional nanostructure fabrication. The self-assembled systems on the surfaces are used with advantage to study the basic principles of the molecular self-assembly by surface analytical methods.

However, the two dimensional molecular assemblies on the surfaces are not only model systems for investigation of the self-assembly process but also exhibit tremendous potential for applications in quantum computing, catalysis, nanofabrication. The main advantage of this bottom-up approach is the combination of atomic precision of prepared structures and scalability of the process unattainable by any of the top down techniques.

The metal-organic networks on a surface are an example of the self-assembled structure where the metal coordination centres are linked by organic ligands. The precise arrangement of the assembly can be employed for investigation of the interaction between the coordination centres that often shows multiple spin states [2]. As was shown recently, the magnetic moments of the spin centres may exhibit long-range order due to substrate mediated interactions [3]. The electronic properties of the substrate can affect magnetic coupling of the metallic spin centres. Therefore, preparation of ordered metal-organic structures on the substrate with tunable electronic properties is of a great interest, as it would allow control of a magnetic interaction of many entangled spin centres. A well known material that is able to change its electronic properties upon application of electric field is graphene. A design of metal-organic networks on graphene is an actual research topic.

This work is focussed on the preparation and the characterization of the self-assembled molecular structures and the metal-organic structures on epitaxial graphene. It is a part of the ongoing project with the ultimate goal to prepare a metal-organic system on graphene and study its magnetic properties by electron paramagnetic resonance techniques. The thesis is in the framework of the project an initial step which probes basic self-assembly properties of the potential ligand molecule and explores the possibility of building a metal-coordinated network. Both studies are performed on the epitaxial graphene on Ir(111), which exhibits properties similar to graphene on insulating substrates.

The structure of the thesis is as follows:

The first chapter is dedicated to the introduction into the field of molecular self-assembly on the graphene substrate. First, molecular interactions are described as they play a crucial role in the self-assembly processes. Then properties of graphene are discussed together with methods of graphene preparation. Next, characteristics of self-assembly structure on the graphene substrate are presented.

## *Introduction*

The second chapter is aimed at the instrument used during the experimental part of the thesis. The ultra-high vacuum system is described in the first section together with various related instruments employed for the preparation of the samples. A description of scanning tunneling microscopy (STM) and low energy electron microscopy (LEEM) follows. We also provide brief description of the used setups. In the final part of the chapter is addressed to the X-ray photoelectron spectroscopy.

The third chapter is dedicated to presentation and discussion of the experimental observations made within the thesis. The properties of the used molecule within the study are described followed by a description of the iridium substrate preparation. Graphene growth and the analyses by LEEM and STM are presented in the next section. Then the study of molecular self-assembly on the graphene substrate is presented. The final part is focussed on the the metal-coordinated network on the graphene substrate.

# 1. Molecular self-assembly on graphene substrate

Preparation of atomically precise structures is the key for an ultimate miniaturization of electronic devices [4], development of new q-bit designs [5] and investigation of interactions taking place at atomic scale [6]. An atomic manipulation is one of the fabrication techniques capable of building structures with atomic precision. The method relies on the capability of scanning probe techniques to precisely move single atoms across a surface. However, this method is very technically demanding and time consuming. Therefore, due to the strictly serial nature of the building process, the use of the atomic manipulation is restricted to fundamental research. On the contrary, molecular self-assembly is a fully parallel process by nature; therefore, it is perfectly scalable.

Molecular self-assembly, as the name suggests, is the spontaneous process of supramolecular structure formation driven by complex molecule-molecule interactions. This thesis is focused on the molecular self-assembly on a surface, where also molecule-substrate interactions play a role. Interactions taking part in the self-assembly process are often relatively weak non-covalent interactions. Due to their weak-nature, it is possible to tune the final structure by the parameters of the self-assembly process (e.g. temperature, duration or deposition rate). Nevertheless, the weak interactions results also in a low stability of the final structure. Details of the particular interactions involved in the self-assembly process will be described in Section 1.1.

A substrate plays the key role in the molecular self-assembly process, as a molecule-substrate interactions are always present. This thesis focuses mainly on self-assembly of molecules on graphene, therefore a detailed description of graphene is given in the section 1.2, followed by introduction of specific effects that are important for molecular self-assembly on graphene described in Section 1.3.

## 1.1. Molecular self-assembly on surfaces

Molecular self-assembly is an intensively studied topic in many fields, namely molecular biology and chemistry as well as surface science and nanotechnology. The understanding of fundamental principles of self-assembly processes is required in order to fully exploit the potential of supramolecular structures, not only in the field of quantum computing, but also in catalysis as well as graphene based electronics. The study of the supramolecular structures can be divided into two main branches according to the dimension of the studied structures.

In three dimensions, the intensively studied topic are metal-organic frameworks (MOF). The MOFs are crystals of organic molecules bound to the metal atoms [7]. These materials can be designed for various applications, thanks to variability of the organic linkers in the structure [8]. However, the structure of MOF materials is rather complicated and number of characterization methods is limited. The structure of MOFs is commonly studied by X-ray diffraction techniques.

In two-dimensions, the number of possible self-assembly motifs is greatly reduced, compared with the three-dimensional systems. This fact facilitates interpretation of the observed structures. Therefore, the studies of two-dimensional self-assembled struc-

## 1. MOLECULAR SELF-ASSEMBLY ON GRAPHENE SUBSTRATE

tures provide valuable information about the self-assembly processes. Moreover, two-dimensional supramolecular structures exhibit interesting properties for application in spintronics, catalysis and nano-structure preparation.

The electrically conductive crystals are the most commonly used substrates for the studies of molecular self-assembly. The use of the conductive substrates opens the possibility to employ the STM for analysis of the self-assembled structure at atomic scale. Moreover, local electronic properties as well as magnetic properties of the molecules inside the supramolecular structure can be probed by methods of the STM. For these reasons, the conductive substrates are used in a majority of the supramolecular structure studies.

Surfaces, where the self-assembly takes place, need to be atomically clean. Therefore, the experiments have to be performed in strictly defined environment. One of the possible environments is a clean liquid solution, the second is ultra-high vacuum. Nevertheless, the preparation of the clean surfaces is very limited in the solution, making the choice of available substrates for the studies in solution rather limited. In contrast, the UHV environment allows to prepare the clean surfaces of various materials. Therefore, it is the convenient environment for the study of molecular self-assembly.

The molecules are thermally evaporated on the sample surfaces placed inside the UHV system. The thermal evaporation techniques allows to precisely control the deposition rate of the molecules on the surface. The deposition rate is one of the factors affecting the resultant supramolecular structure [9]. The second factor is the temperature of the substrate during the deposition. By fine tuning of the substrate temperature and the deposition rate, it is possible to tune the properties of the prepared superstructure [10]. Besides these parameters, the molecular superstructure is determined by molecule-molecule interactions and molecule-substrate interactions. These interactions are described in the following section.

### 1.1.1. Molecular interactions

The interactions taking place in the supramolecular structure formation are weak non-covalent interactions. Generally, an interplay of multiple interactions participate in the structure formation. A description of the main interactions that takes part in the self-assembly process is presented in following paragraphs.

#### Dispersive interaction

The dispersive interactions are a subset of the van der Waals interactions. They act between objects with non-permanent charge distribution [11]. As long as the electrons in the molecules are quantum objects exhibiting quantum fluctuation, the dispersive interactions are always present in molecular systems. Intensity of the interaction is relatively weak compared with other intermolecular iterations. A potential of the dispersive interaction is inversely proportional to the sixth power of the distance from the center, hence it acts only at small distances. The potential is isotropic, therefore it favors a close-packed supramolecular structure with the symmetry reflecting the symmetry of its building blocs [12].

## 1.1. MOLECULAR SELF-ASSEMBLY ON SURFACES

### Hydrogen bond

The Hydrogen bond is an electromagnetic interaction of permanent electric dipoles. Therefore, it takes place only between molecules with functional groups that has certain asymmetry in charge distribution. The functional groups containing a hydrogen atom bound to an element with high electron affinity (O, N, F, etc.) often participate on hydrogen bond, due to the electric dipole formed by asymmetry of the electron density between the hydrogen atom and the element with high affinity.

In contrast to the dispersive interactions, the hydrogen bonds are stronger and directional. Therefore, supramolecular structures with the hydrogen bond dominant over the dispersive interactions are no longer affected by the symmetry of the molecule. However, they preferentially reflect number and position of the groups involved in a formation of the hydrogen bonds.

### $\pi$ - $\pi$ Interaction

The  $\pi$ - $\pi$  interactions comes into play, when  $\pi$  electrons are involved in the system. Therefore, this interaction plays a crucial role in the interaction of aromatic rings, which are often present in the molecular structure. Aromatic ring interact with each other through electrons in p-orbitals oriented perpendicular to the aromatic ring. The  $\pi$ - $\pi$  interaction favours face-to-face orientation of the aromatic rings [13]. Due to the  $\pi$ - $\pi$  interaction, the molecules containing aromatic ring are preferentially oriented with the ring parallel to the graphene or graphite substrate.

### Coordination bond

The interaction of atoms or molecules through delocalized orbitals of coordination center is called the coordination bond [14]. The coordination centers are often formed by an atom or a group of atoms of a transition metal. The transition metal contain unoccupied and highly delocalized d- or f-orbitals that are able to accept and share electrons of bounded ligands. The coordination interaction is directional. The supramolecular structure with dominant coordination interaction reflects the symmetry of the coordination centres and the number and the orientation of the ligand groups of the organic molecules.

Nevertheless, the coordination centers do not have only the structural functionality, but also display interesting properties for application in the catalytic processes. Moreover, thanks to the periodic nature of the molecular superstructure, it is possible to arrange a large number of metallic coordination centers with atomic precision. The coordination centers display multiple spin-states [5]. Therefore, the metal-organic superstructures are prospective for a future development in the field of quantum computing [15].

### Charge transfer

An adsorption of molecules on a surface may lead to the charge transfer between the molecule and the substrate. The charge transfer occurs due to misalignment of the electronic states of the substrate and molecular orbitals of the adsorbed molecule. Electrons in the molecules occupy molecular orbitals, which may be delocalized over the whole molecule. For an interaction of the molecule with the substrate, an energy of the highest occupied molecular orbital (HOMO) and the lowest unoccupied orbital (LUMO) plays the key role.

## 1. MOLECULAR SELF-ASSEMBLY ON GRAPHENE SUBSTRATE

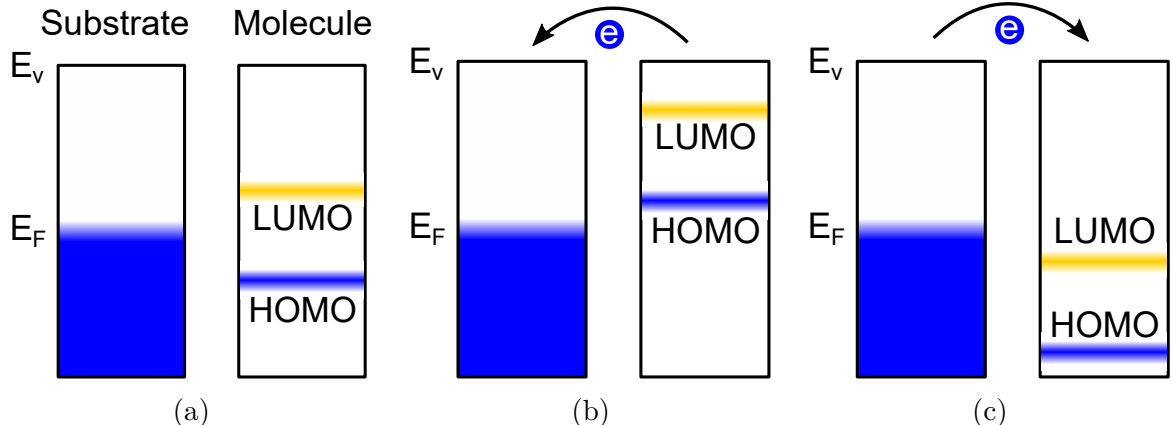


Figure 1.1: Schematics of the energy levels of the adsorbed molecule on the metallic surface. (a) the Fermi level  $E_F$  of the substrate is located above HOMO and below LUMO, in contrast with (b) and (c), where the Fermi level is located below HOMO or above LUMO. In the cases (b) and (c) the charge transfer occurs.

The ionization potential and the electron affinity are energy differences of the vacuum energy level  $E_v$  and HOMO or LUMO, respectively. In the Figure 1.1 the energy diagrams for three different situations of molecular adsorption on a metallic surface are presented. In the case, in which the Fermi level  $E_F$  is located between HOMO and LUMO, the charge transfer between the substrate and the molecule is negligible. It is caused by the fact that the filled HOMO of the molecule is aligned with the filled states in the metal and the empty LUMO is aligned with the empty states in metal. Such case is depicted in Figure 1.1a.

If HOMO of the molecule is above the Fermi level  $E_F$  of the substrate (Figure 1.1b), electron is able to migrate from the molecule to the substrate. Hence, the molecule is positively charged and the substrate is n-doped.

In the last case (Figure 1.1c), in which the LUMO is located below the Fermi level of the substrate, the charge transfer occurs in the opposite direction, from the substrate to the molecule. Therefore, the molecule is negatively charged and the substrate is p-doped.

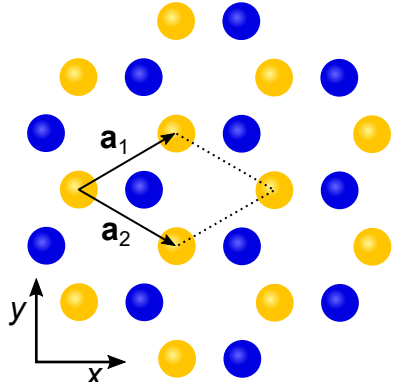
In the systems, where the charge transfer takes place, the attractive interaction between the molecule and the substrate arises from the electrical dipole formation. Moreover, it allows to precisely control doping of 2D materials [16]. Further details related to the charge transfer in molecular systems can be found in reference [17].

### 1.1.2. Kinetics and thermodynamics of self-assembly process

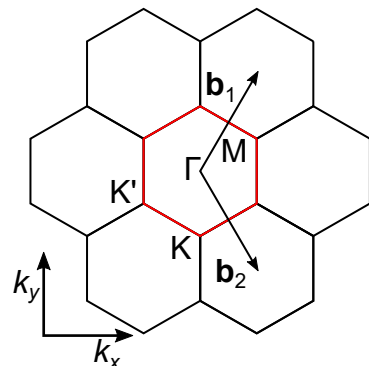
The process of self-assembly is controlled by an interplay between kinetic limitation and the intermolecular interactions steering the system into thermodynamically stable structure. On surfaces, the main factor limiting the formation of supramolecular structure is the surface diffusion of building blocs over the surface, which is required to obtain ordered structure.

Diffusion on the surface obeys an Arrhenius law, which means that the diffusivity – square distance traveled by a molecule across the surface per a unit of time – is exponentially dependent on the temperature as well as on the diffusion barrier of the molecule on the surface. The diffusivity on the surface during the preparation of the ordered structures is controlled by the substrate temperature.

## 1.2. GRAPHENE



(a) Graphene lattice



(b) Reciprocal lattice

Figure 1.2: (a) Schematics of graphene atomic structure. Yellow and blue colors differ two atoms in the basis. The primitive cell is depicted by dashed line and the length of primitive translation vectors is 2.45 Å. The nearest atom distance on the graphene surface is 1.42 Å. (b) Reciprocal lattice of graphene. Red line indicates the edge of the first Brillouin zone. The high symmetry points are labeled by letters  $\Gamma$ , K, K' and M. Points K and K' are so called Dirac points, where the electron dispersion relation is linear.

The second factor that affects the structure of self-assembly on the surface is the deposition rate of the building blocs on the substrate. The deposition rate limits the time, in which the just deposited building block has to find the position with the lowest potential. The Deposition rate is the second factor that can be controlled during the preparation of the supramolecular structures. These effect are in detail described in the reference [9].

## 1.2. Graphene

Graphene is a single layer of carbon atoms arranged into a ‘honeycomb’ lattice. Its electronic structure was described back in 1947 by P. R. Wallace, who was studying a structure of graphite [18]. The work includes also calculations of the electronic structure of a single-layer graphite, a purely theoretical system at that time. Almost 60 years later, in 2004, graphene was experimentally prepared at the University of Manchester [19]. Since then, graphene has become one of the most studied materials thanks to its unique mechanical and electronic properties.

### 1.2.1. Graphene structure

A schematics of graphene crystalline structure is shown in Figure 1.2a, where two sub-lattices differ in color.

Carbon atoms in graphene are bound by strong  $\sigma$  covalent bonds. Therefore, one s-orbital and two p-orbitals of the carbon atom are hybridized to form an in-plane structure of the crystal. The third non-hybridized p-orbital is occupied by single electron. The non-hybridized p-orbital is oriented out of the crystal plane. From mutual interaction of the p-orbitals a  $\pi$ -band arises in the electron dispersion relation of graphene. Electrons in the  $\pi$ -band are able to propagate on long distances without scattering [20], this gives rise to the graphene unique charge transport properties.

## 1. MOLECULAR SELF-ASSEMBLY ON GRAPHENE SUBSTRATE

Electron dispersion relation of the  $\pi$ -band close to the Dirac points (labeled K and K' in Figure 1.2b) is linear and it can be described by relation:

$$E_{\pm}(\mathbf{q}) = \pm v_F |\mathbf{q}|, \quad (1.1)$$

where  $\mathbf{q}$  stands for momentum relative to the Dirac point and  $v_F$  is Fermi velocity [18]. The two signs distinguish between occupied valence  $\pi$ -band ( $-$ ) and unoccupied  $\pi^*$ -band ( $+$ ) that are touching in the Dirac point. The Fermi level of the pristine graphene is precisely at Dirac point.

Due to the striking similarities with the dispersion relation of photon, electrons with the linear dispersion are often called Dirac fermions. The only difference is the speed  $v_F$  of the electrons in graphene, which is roughly  $1 \cdot 10^6$  m/s compared with speed of photon  $3 \cdot 10^8$  m/s. This analogy opens the possibility to probe relativistic effects in the system with the limit velocity lower by factor of 300 [21].

The possibility to tune the position of the Fermi level by external electric field is another property of graphene, which holds a potential for application in electronic industry [19]. By tuning the position of graphene the Fermi level the amount of electrons at the Fermi level is changed and so is the conductivity. The position of the Fermi level plays a key role in electron transfer between the adsorbate (e.g. molecule) and the substrate. Therefore, graphene is a prospective substrate for tunable molecular networks.

Up to now, the properties of graphene were discussed without any consideration of a substrate. However, the substrate is present in almost every real graphene-based system. The electronic and structural properties of graphene are always to some extend affected by the presence of the substrate. Therefore, in next section we discuss characteristic properties of graphene on different substrates together with methods of preparation, which are often *substrate specific*.

### 1.2.2. Graphene on various substrates

Scalable methods of graphene preparation are still subjects of studies, because graphene production is one of the biggest obstacles for a wide range of its applications. The graphene preparation methods can be divided in two groups: top-down and bottom-up methods. Quality of graphene crucially depends on the method of preparation and on the chosen substrate. Different interactions between graphene and substrate take place and therefore affect its transport properties. The charge mobility in graphene is the convenient measure of graphene quality, reflecting overall structural coherency of the crystal together with the amount of scattering impurities. An overview of the charge mobility in graphene for various methods of preparations and different substrates is presented in Table 1.1.

### 1.2.3. Top-Down methods of graphene fabrication

Top-down methods rely on separation of single layer graphene from bulk graphite or pre-processed substrate. The first graphene layer ever experimentally prepared, was exfoliated from graphite by repetitive peeling off layers of highly oriented pyrolytic graphite by a scotch tape [19]. Today, the exfoliation method is known as a method capable to produce the highest quality graphene layers in ambient conditions. Furthermore, the method

## 1.2. GRAPHENE

Table 1.1: Mobility of charge carriers ( $\mu$ ) in graphene fabricated by different techniques on different substrates. Table is adapted from [22].

Substrate	Fabrication technique	$\mu$ ( $\times 10^3 \text{ cm}^2 \text{V}^{-1} \text{s}^{-1}$ )	Ref.
$\text{SiO}_2 / \text{Si}$	Exfoliation	10-15	[19]
Boron nitride	Exfoliation	25-140	[23]
Suspended	Exfoliation	120-200	[24]
SiC	Thermal-SiC	1-5	[25]
$\text{SiO}_2 / \text{Si}$	Cu-CVD	1-16	[26]

is very cheap and does not require any special instruments; this makes it perfect for experimental applications.

Moreover, variety of substrates can be used for devices prepared by exfoliation. One of the most frequently used substrates is silicon-dioxide ( $\text{SiO}_2$ ) layer on silicon wafer due to its insulating properties and possibility to identify monolayer graphene by eye in optical microscope [27]. Drawback of the  $\text{SiO}_2$  substrate is the trapped charge on the graphene-oxide interface. The trapped charge significantly degrades charge transport properties of graphene [28]. Furthermore, a microscopic roughness of the  $\text{SiO}_2$  surface prevents use of graphene as the substrate for molecular systems with the long range order [29]. Therefore, an alternative substrate for the graphene based devices is needed.

Hexagonal boron nitride (hBN) is the recently discovered substrate suitable for the graphene based devices providing numerous advantages over  $\text{SiO}_2$  [23]. First of all, hBN offers atomically flat surface. Hence, the mechanical corrugation of graphene on top of hBN is significantly smaller compared to the corrugation of graphene on  $\text{SiO}_2$ . Furthermore, there are no trapped charges on the interface, which could act as scattering defects for electrons in graphene. Therefore, the charge transport properties of graphene on hBN are similar to those of the suspended graphene [23]. On the other hand, hBN is prepared by exfoliation of single crystals, which restrict its use only for laboratory conditions. However, graphene deposited on hBN is a suitable substrate for a design of self-assembled molecular networks with long-range order, thanks to the high structural coherency of graphene.

Another way to prepare graphene from graphitic materials is micro-mechanical cleaving by sonication [30]. The sonication methods are capable of graphene preparation on a large scale. However, the prepared graphene flakes are often small and suffer from many defects and impurities caused by the chemical treatment. Therefore, graphene prepared by the sonication method can not be used as a substrate for supramolecular structures. A detailed description of this method, which goes beyond the scope of this theses, is given in reference [31].

### 1.2.4. Bottom-up methods of graphene fabrication

In general, the bottom-up methods have the advantage of scalability over the top-down methods, which is also true in case of graphene fabrication. On the other hand, bottom-up methods of graphene preparation often require extreme conditions in terms of temperature and pressure, calling for utilization of a dedicated experimental apparatus. Two groups of

## 1. MOLECULAR SELF-ASSEMBLY ON GRAPHENE SUBSTRATE

bottom-up methods are widely used nowadays: the thermal annealing of silicon carbide (SiC) and the chemical vapor deposition (CVD) of carbon on various substrates.

The principle of graphene growth on SiC substrate lies in the different evaporation temperatures of silicon and carbon from the SiC crystal. During the process, the SiC crystal is heated to temperature  $>1000$  °C, at which silicon is evaporated from the SiC surface. Residual carbon on the surface forms graphite. It is possible to achieve preferential growth of single layer graphite – graphene – by precise selection of the growth conditions. SiC is an insulating material, hence the measurement of the transport properties of graphene is possible directly on the samples, without a need for transfer of graphene to a different substrate. Also, this method is well scalable and suitable for wafer scale production, due to good availability of SiC substrate, which is already a well established material in semiconductor industry for high power applications. Graphene growth on the SiC substrate is epitaxial. The growth is possible on two SiC surfaces, namely SiC(0001) and SiC(0001̄). Therefore, it is necessary to use monocrystalline substrates, which significantly increase the production costs of this method. Still, epitaxial growth of graphene on SiC is a prospective way for the large scale production.

The epitaxial growth on SiC uses the substrate itself as a source of carbon atoms. The second group of methods for graphene preparation based on the CVD employs an external source of carbon atoms in form of a carbon containing compound, so called precursor. The precursors can be used in form of solid or liquid [32], but gaseous materials are the most frequently used.

During the CVD, molecules of the precursor are decomposed at high temperature and subsequently carbon atoms are either dissolved in a substrate or directly form a graphene layer on top of the substrate. The mechanism depends on solubility of carbon in a substrate material. Commonly used substrates for CVD graphene growth are transition metals such as Fe [33], Rh [34], Cu [35], Ni [36] or Ir [37]. The growth mechanism is substrate specific. In general, two factors have to be taken into account; the first one, is the catalytic behavior of the substrate in the precursor molecule decomposition reaction and the second is the solubility of carbon in the material of the substrate. Next, we discuss a few examples of frequently used substrates for the graphene growth.

The most substrate is polycrystalline copper, which is widely used, due to its good availability and low price compared to other transition metals. The solubility of carbon in copper is low at a process temperature (approx. 1300 K) [38]. Decomposition of gaseous carbon precursor is catalyzed by the copper surface. Therefore, in principle, the growth of graphene on the copper substrate should be self-limited to single monolayer [35]. However, the growth of multilayer graphene on copper is frequently observed [39]. The growth mechanism of multilayer graphene was recently explained by an interplay of copper sublimation and diffusion of carbon under the already grown layer of graphene [40].

The second most used metal, nickel, has significantly higher solubility of carbon. Therefore, the growth mechanism is different on its surface. The growth process consists of two steps. In the first step, the substrate is enriched with carbon from the precursor. During the second step, the substrate is cooled down and the solubility of the carbon in nickel decreases. In order to reach the new equilibrium concentration, the carbon atoms from the bulk material segregate on the surface forming a graphene layer. This process is not, in principle, self-limited to the single layer graphene growth. Therefore, precise control of the process is required to grow large scale single layer graphene.

## 1.2. GRAPHENE

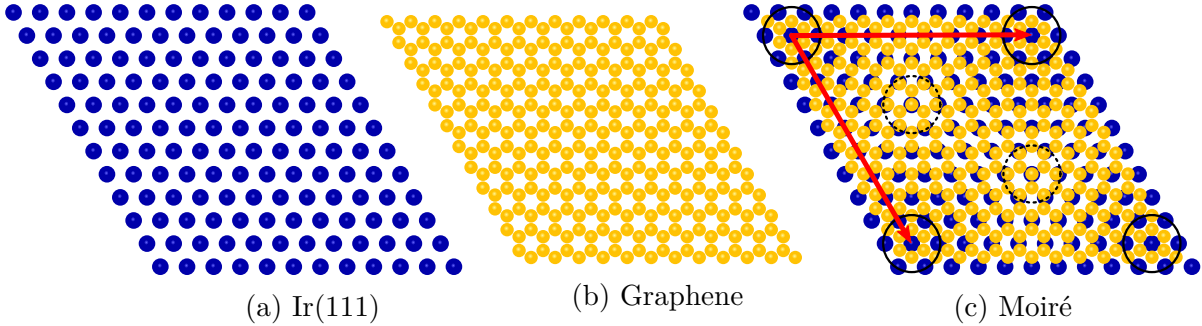


Figure 1.3: (a) Schematics of atomic structure of iridium (111). (b) Schematics of graphene structure. (c) Schematics of graphene on iridium surface (111) showing moiré pattern. The circles mark atop (full line) and hollow (dotted line) adsorption sites within moiré unit cell. The primitive translation vectors of the moiré pattern are labelled by the red arrows. Nearest atom distance on iridium surface is  $2.715\text{ \AA}$  and length of graphene lattice vector is  $2.461\text{ \AA}$ .

Neither of the presented growth mechanisms requires the epitaxial growth, hence the used substrates can be polycrystalline. However, for the growth of monocrystalline graphene with the determined orientation to the substrate the metal single crystal is required. The structure of epitaxial graphene strongly depends on the interaction with the substrate and relative orientation of the substrate surface and the graphene layer. In the next section we discuss only graphene on iridium (111), which was used as substrate for molecular structures within this thesis. Detail description of graphene on other materials can be found in the reference [41].

### 1.2.5. Graphene on iridium

Iridium is a metal with a face-centered-cubic (fcc) structure. The (111) surface of the iridium crystal is used for the graphene growth. Six-fold symmetry of the surface together with the nearest atomic distance of 2.715 Å facilitate the epitaxial growth of graphene. Hence, it is possible to maintain the same crystallographic orientation of graphene on the iridium surface, which results in well defined properties of the graphene on the substrate.

Graphene on iridium is a well-known example of a system with low interacting graphene [42]. Graphene in this system interacts with the substrate only by the weak van der Waals interaction. The interaction defines the preferential orientation of graphene to the substrate, but it does not significantly modify the unique electronic structure of graphene. Therefore, the electronic structure of graphene on iridium is very similar to the structure of free-standing graphene, or graphene on many insulating substrates.

Characteristic for graphene on iridium is a periodic variation of properties called moiré effect shown in Figure 1.4. The moiré is the effect caused by the small misfit of lattice vectors of iridium and graphene. The misfit results in a periodic variation of relative position of carbon atoms with respect to the surface atoms of iridium. Two different positions of a graphene hexagon relative to the substrate atom can be distinguished: an atop site and a hollow site. Carbon atoms in the vicinity of the atop sites are located further from the substrate atoms compared to the position of carbon atoms around the hollow sites. Hence, the interaction of the carbon atoms with the substrate is weaker in areas close to the atop sites compared with the interaction around the hollow sites.

## 1. MOLECULAR SELF-ASSEMBLY ON GRAPHENE SUBSTRATE

A magnitude of a reciprocal vector  $k_{\text{moiré}}$  of the moiré pattern might be calculated from the reciprocal vectors of the graphene lattice  $k_{\text{gr}}$  and iridium lattice  $k_{\text{Ir}}$  by relation:

$$k_{\text{moiré}} = k_{\text{gr}} - k_{\text{Ir}}. \quad (1.2)$$

If we assume  $k_{\text{gr}} = 2\pi/2.461 \text{ Å}^{-1}$  and  $k_{\text{Ir}} = 2\pi/2.715 \text{ Å}^{-1}$ , the calculated moiré reciprocal lattice constant is  $k_{\text{moiré}} = 0.2389 \text{ Å}^{-1}$  corresponding to the periodicity of the moiré pattern  $26.30 \text{ Å}$ . The calculated value is in agreement with the experimentally observed value [43].

The moiré pattern is not observed exclusively on graphene on iridium, but it is a general effect of the lattice mismatch of epitaxially grown layers. The relation of the moiré periodicity with the reciprocal vectors of two overlaying lattices opens a possibility to resolve the lattice mismatch in a great detail. Furthermore, the moiré as a periodic modification of the graphene properties allows to selectively modify graphene in particular areas of a moiré unit cell. Therefore, the moiré is playing the key role in adsorption of molecules on the graphene substrate, as was demonstrated in [44].

### Graphene growth on iridium

There are two well established techniques for graphene growth on iridium: the temperature programed growth (TPG) and the CVD. Both the techniques use ethylene gas as source of carbon during the process.

During the TPG, ethylene is preadsorbed on the substrate surface at room temperature. Subsequently, the substrate is annealed at high temperature (approx. 1200 K), in order to decompose the precursor. Finally, from the carbon atoms remaining on the surface, graphene islands are formed. The shape and morphology of the formed graphene islands depend on the annealing temperature during growth. The morphology of graphene islands vary from numerous small islands formed at the low annealing temperatures (approx. 900 K) to large separated island growing at the high temperatures (approx. 1470 K) [37]. The TPG has an advantage of simplicity as only the annealing temperature plays the key role in the growth procedure. However, nature of TPG process does not allow growth of continuous graphene layer, which is only possible by CVD method.

During the CVD, the precursor is dosed on an already hot iridium surface, where it is decomposed and residual carbon atom form graphene layer on the surface. By precise control of the growth parameters, it is possible to grow a complete monolayer of graphene. However, for the grow of monocrystalline graphene layer, high temperatures (approx. 1530 K) during growth process are necessary [45].

At lower growth temperatures, the graphene layer is polycrystalline with various crystal orientations relative to the iridium surface orientation. However, millimeter-scale graphene monocrystals are achievable by a combination of the TPG and the CVD growth at lower temperatures [46]. In the combined process the precursor is adsorbed on the surface at room temperature and subsequently the sample is heated to approx. 1110 K in the precursor atmosphere. Therefore, oriented graphene islands are grown from the preadsorbed precursor and are further extended by the CVD growth. It is possible to grow millimeter-sized single crystalline graphene by this procedure.

### 1.3. GRAPHENE AS A SUBSTRATE FOR MOLECULAR SELF-ASSEMBLY

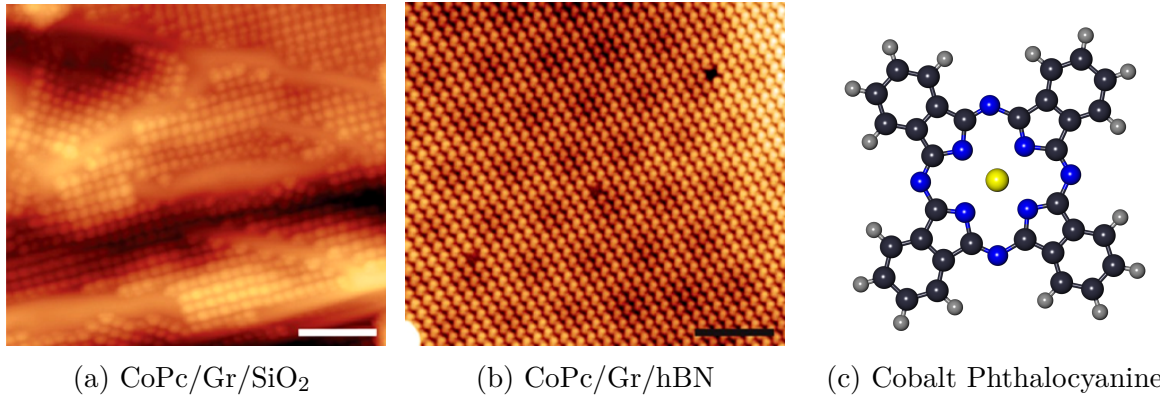


Figure 1.4: STM observation of supramolecular structure on graphene (Gr) on (a) SiO<sub>2</sub>, (b) hBN. Difference in roughness of the substrates is more than an order of magnitude. Scale bars are 10 nm. Adapted from [29]. (c) Model of CoPc molecule. Molecule consists of carbon (black), hydrogen (gray), nitrogen (blue) and cobalt (yellow) atoms. The molecular structure of CoPc is planar.

## 1.3. Graphene as a substrate for molecular self-assembly

The self-assembly on a graphene substrate is a perspective field, because it offers a possibility to control the graphene electronic properties by the physisorption of molecules on the graphene substrate. Graphene is also the ideal substrate for a study of supramolecular structures. Thanks to the low reactivity of graphene, design of superstructures with dominant molecule-molecule interaction is possible. Moreover, the possibility to change graphene charge carrier concentration by an external electric field, makes graphene a prospective substrate for the tunable supramolecular structures growth. Nevertheless, for external tuning of the electronic properties, graphene has to be placed on an insulating substrate, which makes process of graphene preparation technically demanding. Therefore, vast majority of studies focuses on the self-assembly properties on the in-situ grown epitaxial graphene on metallic substrate (mostly Ir(111) and Ru(0001)) or the insulating SiC crystals.

### 1.3.1. Molecular self-assembly on graphene on insulating substrate

Self-assembly properties of organic molecules on two insulating substrates have been shown by Järvinen et al. [29]. Authors used the low-temperature STM to study the supramolecular structure of cobalt phthalocyanine (CoPc) on CVD graphene on SiO<sub>2</sub> and hBN substrates prepared in UHV. On both substrates, the superstructure exhibits four-fold symmetry emerging from the symmetry of the molecule. The four-fold symmetry is caused by a weak molecule-substrate interaction compared with a molecule-molecule interaction.

However, in the case of graphene on SiO<sub>2</sub>, the supramolecular structure is significantly disordered due to the surface roughness of the SiO<sub>2</sub> layer and the long-range order is not present in the supramolecular structure. Measured corrugations of graphene on SiO<sub>2</sub> are

## 1. MOLECULAR SELF-ASSEMBLY ON GRAPHENE SUBSTRATE

up to 1 nm. The corrugations also gives a rise to inhomogeneous charge transfer between adsorbed molecules and graphene.

The charge transfer between a molecule and graphene is not important only for the study of supramolecular structure, but it also provide the method for tuning the charge carrier concentration in underlying graphene. Study of charge transfer between graphene and 1,3,5-Tris-(2,2-dicyanovinyl)benzene (CVB) molecule has been presented [47]. Authors prepared the CVB supramolecular structure on CVD graphene transferred on a hBN/SiO<sub>2</sub>/Si substrate. The Si back electrode allows to apply a bias electric field perpendicular to the graphene plane. The change of the relative position of the Fermi level and molecular orbitals has been demonstrated upon application of the bias electric field. Hence, the experiment shows the possibility to prepare a molecular superstructure with properties tunable by the applied electric field.

### 1.3.2. Graphene moiré and molecular superstructure

The substrate used for the graphene growth has an important effect on the molecular superstructure formed on the top of graphene. This effect is mainly caused by the moiré pattern of graphene and the substrate. The moiré brings a periodic corrugation of graphene together with changes in its electronic structure. Therefore, the moiré pattern affects the preferential adsorption sites of molecules on the graphene surface.

The effect is obvious in comparison of two CoPc supramolecular structures on graphene epitaxially grown on two different substrates: Ru(0001) and Ir(111). Graphene strongly interacts with the Ru substrate, hence the moiré pattern on Ru is more pronounced compared with graphene on the Ir substrate, the interaction of graphene and the Ir substrate is weaker.

The supramolecular structure on graphene on the highly interacting Ru substrate reflects six-fold symmetry of the moiré pattern [48], whereas the supramolecular structure of the same molecule on graphene on Ir is close-packed with four-fold symmetry reflecting the symmetry of the CoPc molecule [49].

This behavior can be explained by variation of the work function of graphene across the unit cell of the moiré pattern. The local variation of the work function induces an in-plane electrical dipole. The electric dipole interacts with an induced dipole of the molecule and guides the molecule into a specific binding site within moiré unit cell [50].

The adsorption properties modified by graphene moiré can be used for preparation of structures with long-range order. This principle was employed in recent study for building periodic structures of fullerene C<sub>60</sub> on graphene on Ru(0001) [44]. Graphene moiré acts as a template for the growth of self-assembled structures.

## 2. Experimental methods

The study of new molecular structures requires a precisely controlled environment. Therefore, all experiments within this thesis are performed in the ultra high vacuum (UHV). The UHV offers a possibility to prepare and maintain atomically clean surfaces, which can be used as precisely defined substrates for the preparation of the molecular systems. For cleaning of the substrates, we employ a combination of ion sputtering and high temperature annealing. Details of the substrate cleaning procedures are further described in Chapter 3 along with a process of molecular system preparation. A brief description of the UHV apparatus used within this thesis is given in the first section (2.1).

The second section (2.2) is dedicated to the scanning tunneling microscopy (STM). The STM is the scanning probe technique that offers a unique spatial resolution. The high spatial resolution allows to resolve structures at the atomic scale. This feature is desirable for a study of molecular systems. The STM opens possibilities to resolve a single building blocks of a complex system. Therefore, an interpretation of the processes ongoing on the surface is significantly facilitated.

In Section 2.3, the low energy electron microscopy (LEEM) is discussed. The LEEM is an electron microscopy technique with a unique surface sensitivity. Moreover, the method is able to image structures with long-range order such as the supramolecular structure and distinguish between different orientations of the structure. Another strength of the LEEM is its capability to *in-situ* observe processes at temperatures up to 1500 K. This allows to observe the epitaxial graphene growth on the iridium substrate or structural transformations of molecular systems at elevated temperatures.

In the last section, the X-ray photoelectron spectroscopy (XPS) is described. The XPS is a commonly used technique for a surface chemical analysis. A bonding environment of each element can be determined by this method. As the bonding environment of metal atoms is significantly different in a bulk metal compared with a metal-organic structure, formation of the metal-organic molecular superstructure can be identified by the XPS. Description of the XPS method is presented in Section 3.10.

### 2.1. The ultra-high vacuum apparatus

All experiments presented within this thesis were performed in a UHV cluster. The UHV cluster is situated in the laboratories of CEITEC Nano Research Infrastructure. Schematics of the cluster is shown in Figure 2.1. The cluster consists of nine chambers interconnected by a linear transfer system (TS). The base pressure of the TS is  $<5\cdot10^{-10}$  mbar. Therefore, it allows to transport atomically clean samples between the chambers within the UHV. The chambers are connected to the TS via a vacuum tight gate-valves, hence the vacuum in the TS is not affected by processes performed in the attached chambers. The chambers used for the preparation and the analysis of the supramolecular structures have a base pressure  $<5\cdot10^{-10}$  mbar. Vacuum in the chambers is sustained by a combination of turbo-molecular, titanium-sublimation and ion-getter pumps. The samples are introduced into the system via a load-lock chamber.

Cleaning of the samples is performed in a preparation chamber (PC). The PC is equipped with a broad-beam ion sputter-gun, an electron-beam heater, an O<sub>2</sub> needle-valve

## 2. EXPERIMENTAL METHODS

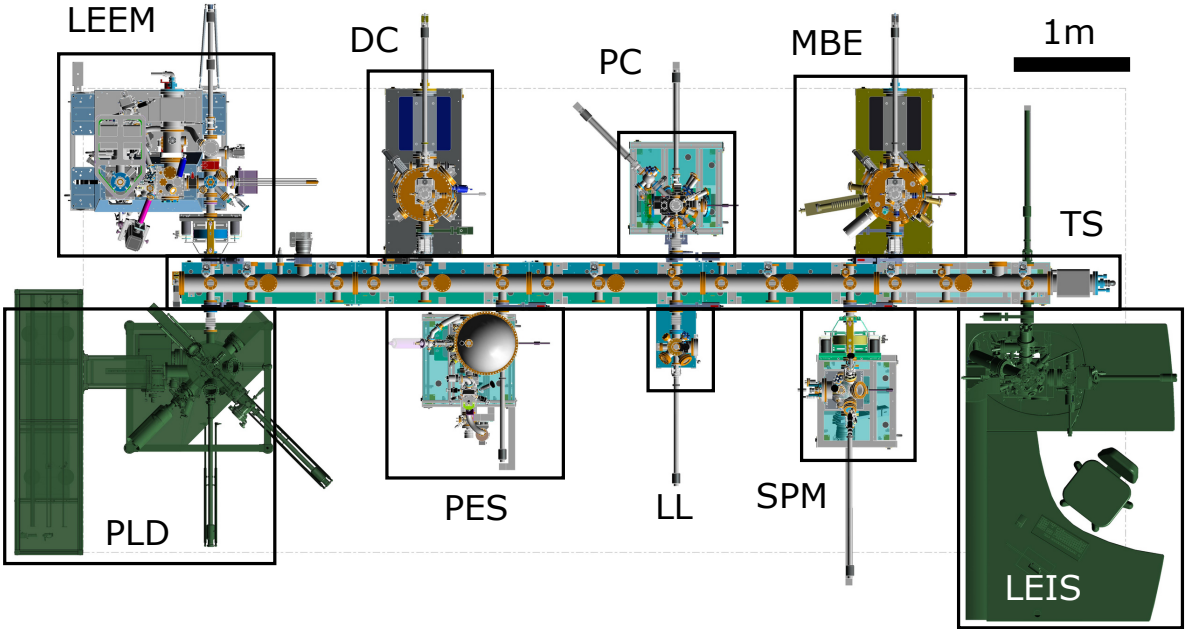


Figure 2.1: Schematics of the UHV cluster. The components are labeled in the schematics as follows: the low energy electron microscopy setup (LEEM), the deposition chamber (DC), the preparation chamber (PC), molecular beam epitaxy chamber (MBE), the linear transfer system (TS), the low energy ion scattering setup (LEIS), the scanning probe microscopy setup (SPM), the load-lock chamber (LL), the photo-electron spectroscopy setup (PES) and the plasma laser deposition setup (PLD).

and an electron optics designed for low energy electron diffraction (LEED) observations. The ion sputter-gun is an electron-impact ion source which is able to produce ions of Ar with a kinetic energy in a range of 0.5-3 keV. The  $\text{Ar}^+$  ions are accelerated towards the sample, where they sputter the material away. This method is used for cleaning of the substrates. The electron-beam heater is built in a manipulator of the PC. A thoriated tungsten filament, placed behind the sample, is used as a source of electrons. The filament is heated by an electrical current (approx. 2 A). A negative bias (0-1000 V) is applied on the filament, hence the electrons thermally emitted from the filament are accelerated towards the back side of the grounded sample. The sample can be heated up to 1500 K by the electron bombardment. Annealing of the sample is used in order to reconstruct the sample surface after the sputtering procedure. The annealing temperature is monitored by a pyrometer mounted on a view port of the PC. The  $\text{O}_2$  needle-valve allows to set a partial pressure of oxygen in the PC. Hence, it is possible to anneal the sample in the oxygen atmosphere, which is a convenient method for removing carbon impurities from metal substrates. The structure of the sample surface can be routinely checked by the LEED between individual steps of the cleaning procedure.

The deposition chamber (DC) is designed for preparation of thin films. Multiple electron-beam evaporators, an oil-heated effusion cell and a quartz crystal microbalance (QCM) are present in the DC. A material for evaporation is placed inside the electron-beam evaporator. The material can be in the form of rod or powder in a crucible. During the deposition, the material is heated by an electron bombardment. The material evaporates and flows out from the evaporator. A fraction of the evaporated atoms are ionized by the electrons that heat the material. The ionized atoms can be detected on the outlet

## 2.2. SCANNING TUNNELING MICROSCOPY

of the evaporator as a beam current. The beam current is proportional to the flux of the evaporated atoms. The evaporated atoms condense on the sample that is placed near the outlet of the evaporator.

In the case of the oil-heated effusion cell, the principle of the deposition is the same, except for the heating, which is done by pre-heated oil. The oil is circulating between an electric heater and the effusion cell. The oil in the circuit has high thermal capacity, hence a stability of the temperature during the evaporation is achievable. The oil-heated effusion cell is used for a deposition of organic molecules, on the other hand the electron-beam evaporator is used for deposition of metals.

The beam current measured in the electron-beam evaporator can be correlated with the deposition rate on the sample by the QCM measurements. The heart of the QCM is a piezo-electric crystal that oscillates on its resonant frequency. As the material is deposited on the oscillating crystal, the resonant frequency of the crystal changes. From the changes, the actual deposition rate can be calculated.

In the following sections, the instrument used for the analysis of the samples is described, namely: the STM, the LEEM and the XPS.

### 2.2. Scanning tunneling microscopy

The STM is a method based on a quantum tunneling of electrons between two electrodes. The method was presented for the first time by Bining et al. in 1982 [51]. In the STM configuration, electrons tunnel across a potential barrier between an atomically sharp tip and a sample. The tunneling current  $I_t$  of the electrons is used as a signal for a feed-back loop during experiments. Hence, only electrically conductive samples can be investigated by the STM technique. The tunneling current across the barrier is driven by a bias voltage  $V_b$  applied between the tip and the sample. The feed-back loop of the STM adjusts the tip-sample distance in order to maintain the tunneling current constant. The adjustments need to be very precise, because the tunneling current strongly depends on the tip-sample distance. For example, typical parameters used for the STM measurements are  $V_b = 100 \text{ mV}$  and  $I_t = 1 \text{ nA}$ . The tip-sample distance is approx.  $5 \text{ \AA}$  for these parameters. The precise movements are achieved by piezo-electric actuators. The main part of the actuator is a piezo-electric crystal that changes its shape upon application of an electric field. Therefore, when the bias is applied on the electrodes, which are deposited on the piezo-electric crystal, the crystal elongates or shrinks. The piezo-electric actuators are capable of picometer movements.

An topography related image is obtained by scanning of the tip across the sample surface. There exist two different modes. Both are based on the fact, that the tunneling current depends on the tip-sample distance. In the first, the constant current mode, the feed-back loop is closed. Therefore, the tunneling current is kept constant during the scanning by adjusting a tip-sample distance. The displacements that are required to keep the current constant, are saved and they form a topography-related image of the sample. In the constant height mode, the feed-back loop is open. The tip-sample separation is not adjusted, so the tunneling current varies across the scan. The current variations are saved and they can be also related to the topography of the sample. The constant current mode is used in most of studies because, compared with capabilities of the constant height approach it allows to image surfaces with relatively large corrugations. Moreover,

## 2. EXPERIMENTAL METHODS

the constant height mode requires high thermal and mechanical stability of the STM setup, because the tip-sample position needs to be kept fixed in the range of picometers, otherwise the tip crashes into the sample during scanning.

The key aspect of the STM technique is the quantum tunneling effect. Therefore, in the following section is shown a detailed description of tunneling of an electron across a rectangular potential barrier.

### 2.2.1. Quantum tunneling effect

Assume a problem in one dimension. An electron with the energy  $E$  is incident on a rectangular potential barrier of finite width  $d$  and height  $V_0$  which is described by a potential  $V(z)$ :

$$V(z) = \begin{cases} V = 0 & z < 0 \\ V = V_0 & 0 < z < d \\ V = 0 & z > d. \end{cases} \quad (2.1)$$

To describe the electron in the potential  $V(z)$ , it is necessary to solve the time independent Schrödinger equation, which can be written in the form:

$$\left( -\frac{\hbar^2}{2m} \frac{d^2}{dz^2} + V(z) \right) \psi(z) = E\psi(z), \quad (2.2)$$

where  $m$  stands for the mass of the electron and  $\hbar = h/2\pi$  is the reduced Planck constant. We find the solution of Equation (2.2) in three distinct intervals according to the value of  $V(z)$ . The solution is:

$$\psi_1 = A \exp(ikz) + B \exp(-ikz) \quad \text{for } z < 0 \quad (2.3)$$

$$\psi_2 = C \exp(-\kappa z) + D \exp(\kappa z) \quad \text{for } 0 < z < d \quad (2.4)$$

$$\psi_3 = E \exp(ikz) \quad \text{for } z > d, \quad (2.5)$$

where  $k = \sqrt{2mE/\hbar^2}$  is the wave number of the incident electron.  $\kappa$  which is defined as  $\kappa^2 = 2m(V_0 - E)/\hbar^2$ , is the inverse decay length of the wave function inside the barrier. Amplitudes  $A, B, C, D$  and  $E$  can be determined from the assumption of continuity of the wave function together with its first derivation. The amplitude  $A$  describes the probability of finding an electron propagating towards the potential barrier and  $E$  describes the probability of finding the electron behind the barrier. Hence, the transmissivity of the barrier can be written as:

$$T = \frac{|E|^2}{|A|^2} = \frac{4k^2\kappa^2}{4k^2\kappa^2 + (k^2 + \kappa^2)^2 \sinh^2(d\kappa)}. \quad (2.6)$$

The width of the potential barrier corresponds to the distance between the tip and the sample in the STM configuration. The height of the barrier is given by the work function  $\Phi$  of both electrodes. The work function is defined as the energy necessary for the electron to escape from Fermi level to the vacuum. In case the work function of the both electrodes is not the same, the potential barrier is not rectangular, but it is trapezoidal. In further description we assume both electrodes, the tip and the sample, are made of the same material. Hence,  $\Phi_s = \Phi_t = \Phi$  and the barrier is rectangular. If the Fermi level of the

## 2.2. SCANNING TUNNELING MICROSCOPY

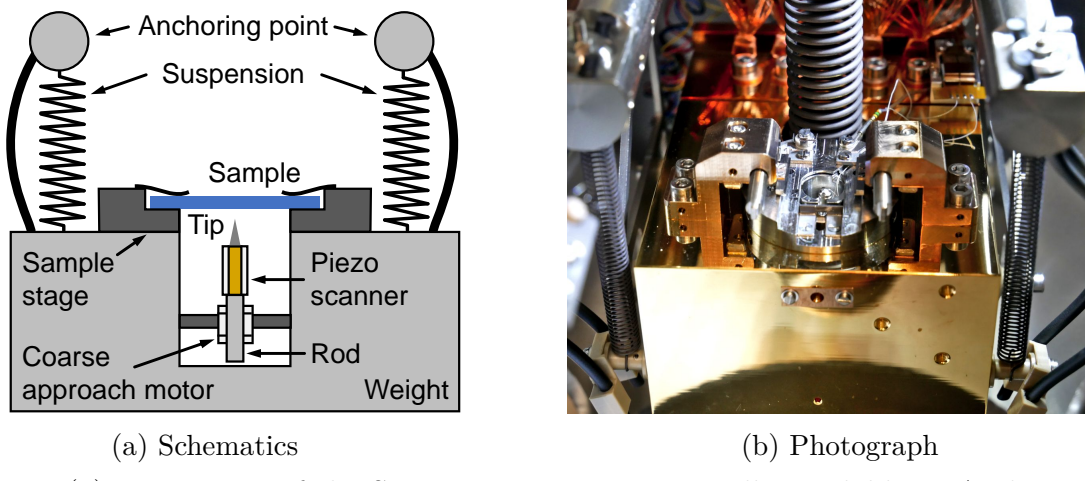


Figure 2.2: (a) Main parts of the STM apparatus commercially available as Aarhus 150 from SPECS, GmbH. (b) Photography of the STM apparatus mounted in the UHV chamber.

first electrode is aligned with the Fermi level of the second electrode, the net tunneling current does not occur. If the bias  $V_b$  is applied, the Fermi levels have the difference in energy  $\Delta E = eV_b$ . Therefore, the electrons from the negatively biased electrode are able to tunnel into the empty states of the other electrode. The tunneling current is proportional to transmissivity of the tunneling barrier. The barrier can be approximated by the rectangular barrier, if the decay length is small compared to the width of the barrier ( $d \gg 1/\kappa$ ). The transmissivity of the barrier (2.6) in this approximation can be expressed as:

$$T \approx \frac{16k^2\kappa^2}{(k^2 + \kappa^2)^2} \cdot \exp(-2\kappa d), \quad (2.7)$$

which is valid for the STM experiment. In the (2.6), the strong exponential dependency of the transmissivity on the parameters of the tunneling barrier is illustrated. Due to the decay length of the electron wave function  $1/\kappa \approx 1 \text{ \AA}$  which corresponds to the typical experimental parameters ( $V_b = 0.1 \text{ V}$ ,  $V_0 = 4 \text{ eV}$  and  $d \approx 5 \text{ \AA}$ ), the tunneling current drops by one order of magnitude when the tip-sample separation is increased by  $1 \text{ \AA}$ .

This properties of tunneling junction ensure the unique combination of spatial and energy resolution of the STM technique. However, high demands on mechanical and thermal stability come along with the high sensitivity.

### 2.2.2. Instrument

The experimental setup used for the characterization of a molecular systems within this thesis is build around Aarhus 150 available from SPECS, GmbH. The Aarhus design was originally developed at University of Aarhus, Denmark. General description of the STM instrument is given in this section. However details of the STM body design can be found in references [52, 53].

The main parts of the STM body are shown in Figure 2.2a along with a photo of the system mounted in the SPM chamber (Figure 2.2b). The STM has a relatively compact design. The STM body is hanged on three springs attached to steel tubes, which are firmly connected to DN 150CF flange. A scanner unit is mounted together with a coarse

## 2. EXPERIMENTAL METHODS

approach motor inside a massive metal block. The mass of the block ensures sufficiently low resonant frequency of the spring-based vibration damping system. At the same time, the block provides a rigid base for the scanning unit. A sample is spring-clamped to the stage which is mounted on the metal block. The stiff mechanical connection of the sample to the microscope body further eliminates mechanical oscillations between the tip and the sample. The tip is attached to the scanning piezo, which is glued to the rod driven by the coarse approach motor.

The motor is the inchworm design, built around a three section piezo tube. The rod is tightly fitted to the inner diameter of the piezo tube. The top and bottom parts of the piezo tube are able to clamp the rod inside, whenever the voltage is applied to the section. The middle part of the piezo tube is able to extends or shrinks in axial direction, upon voltage application. Therefore, the rod fitted into the piezo tube can be moved in axial direction by application of voltage pulses to the piezo tube. A detailed description of the inchworm step motor is available in reference [54].

The key feature of Aarhus design is the exceptional mechanical stability of the setup, which is achieved by the unique compact inchworm coarse approach motor. Resistance to external vibration and compact design allow to operate the microscope even in the noisy environment of the complex UHV cluster. The chamber, where the STM is mounted, is labeled SPM in Figure 2.1.

### 2.3. Low energy electron microscopy

The second method used for the system characterization within this thesis is LEEM. Use of this method for a study of molecular systems is convenient, especially, because its capability to *in-situ* observe on-surface processes at various conditions in real time. Another strength of the LEEM technique is a possibility to easily switch between observation of low energy electron diffraction (LEED) in the reciprocal space and direct imaging in the real space. This feature is especially useful for studies of structures with long range order, for example molecular superstructures. Presented experiments are performed on a commercially available setup FE-LEEM P90 produced by SPECS. The design and principle of operation is described in the next section.

#### 2.3.1. LEEM instrument

The LEEM apparatus can be divided into two separated columns. In the illumination column, an electron probe is formed. The imaging column magnifies and transfers an image of a sample on a detector. Furthermore, by adjustments of the magnetic lenses in the imagining column, it is possible to switch between LEED experiments and imaging in the real space on-sight. Both columns are interconnected by a magnetic prism, which serves as a beam splitter separating the imaging and the illuminating beams. Schematics of the whole system is presented in Figure 2.3.

Probe electrons are emitted from a cold cathode by the field emission. Subsequently, the electrons are accelerated to the energy of 15 keV by the negative potential relative to the rest of the column. An electron beam is formed with use of a series of gun lenses inside the illumination column. The magnetic prism is used to direct the beam into an objective lens, which focuses the beam onto the sample. The sample is kept at a high negative

### 2.3. LOW ENERGY ELECTRON MICROSCOPY

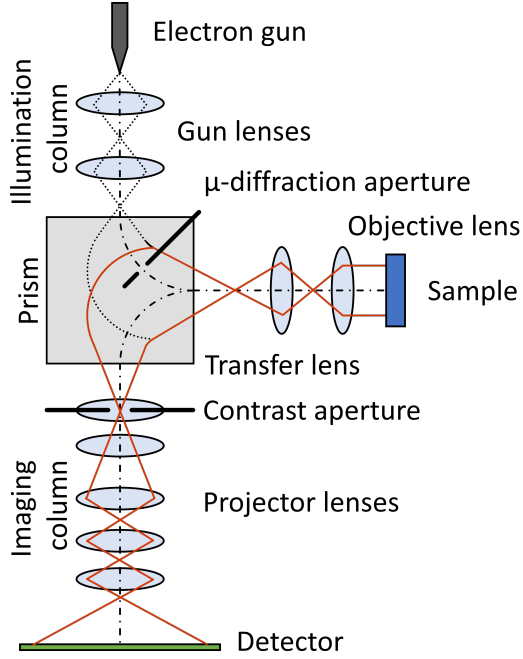


Figure 2.3: Schematics of electron optics of the LEEM setup. Dash dot line shows central ray through whole optical system. Doted lines shows illumination beam and orange line shows image beam.

potential relative to the objective lens. Therefore, the electrons are decelerated by the electric field between the lens and the sample. An impact energy of the electrons is given by a potential difference between the electron gun and the sample. Electrons scattered by the sample are again accelerated by the electric field and collected by the objective lens. The transfer lens transfers the image through the prism to the imaging column. The imaging column magnifies the image onto a detector. As the detector, a combination of a micro channel plate (MCP) and a fluorescent screen is used. The MCP significantly increases the sensitivity of the detector by multiplication of the electrons impacting the fluorescent screen. The screen is monitored by a CCD camera.

The illumination beam can be spatially limited with a  $\mu$ -diffraction aperture placed on the diagonal of the prism. The aperture allows to restrict the illuminated area of the sample down to 185 nm. This feature is especially useful for the LEED experiments, where the diffraction pattern can be obtained only from an area limited by the aperture.

The imaging beam can be restricted by a contrast aperture placed in the imaging column. This aperture has multiple purposes. It allows to control the entrance angle of the objective, hence it gives a possibility to improve the resolution of the microscope by limiting the effect of a spherical aberration. However, the main purpose of the aperture is to perform, the so called, dark-field imaging where the image on the detector is formed only by the electrons scattered into a selected angle. This is possible due to the placement of the aperture in the plane optically conjugated with the focal plane of the objective lens. Further details of the presented microscope can be found in reference [55].

### 2.3.2. Imaging modes of LEEM

The LEEM can be operated in many different modes offering a wide range of information about the probed sample. The simplest imaging mode is the photo emission electron microscopy (PEEM) employing only the imaging column of the setup. The method is based on collecting electrons emitted after absorption of an electromagnetic radiation. The contrast in the PEEM image originates from the local variation of the surface electron emissivity. This method is used during the alignment of the imaging optics of the LEEM setup, because it excludes effects of the illumination optics. A simple UV lamp or synchrotron light source can be used as the source of electromagnetic radiation. The only condition is that the energy and the brilliance of the emitted radiation is high enough to emit sufficient amount of electrons from the sample surface.

The PEEM technique probes occupied energy states of the sample, because it is necessary to emit the electrons from the sample. On the other hand, the LEEM probes empty states above the vacuum level. The contrast in LEEM arises from differences in scattering and reflectivity properties of the surface. In the LEEM we distinguish two different imaging modes: the bright-field and the dark-field. In the bright-field, only the electrons scattered perpendicular to the sample surface participate on image formation. On the contrary in the dark-field, only the electrons scattered into particular angle participate on the image formation. The dark-field mode is especially useful for analysis of the systems where several orientation domains coexist on the surface. As the technique gives a possibility to observe contrast between them. The contrast is achieved by the selection of the diffraction spot corresponding to one orientation of the structure. Hence, only areas that reflect the electrons into the selected direction appear bright in the resultant image. Additional details related to the contrast interpretation in LEEM experiments can be found in reference [56].

## 2.4. Photoelectron spectroscopy

The photoelectron spectroscopy is a method based on energy measurements of the electrons emitted from a sample upon irradiation by photons. During the photoelectron spectroscopy experiment, the probed sample is illuminated with high energy photons. The illuminating photons with energy  $h\nu$  can excite the electrons in the sample above the vacuum energy level. Hence, the excited electron leave the material with a kinetic energy  $E_k$  given by relation:

$$E_k = h\nu - E_b, \quad (2.8)$$

where  $E_b$  is a binding energy of the electron in the material. This simple relation is a link between the measured kinetic energy of the emitted electrons and the sample electronic structure.

Depending on a source of photons, the photoelectron spectroscopies can be divided into two categories. An ultraviolet light sources are used for probing the electrons at energy levels close to the Fermi level and the method is called ultra-violet photoelectron spectroscopy (UPS). On the other hand, properties of electrons at core-levels which are energetically deep below the Fermi level can be analysed upon irradiation with X-ray photons by XPS. Although, the mentioned methods have very similar principle, they provide completely different information about a sample. The UPS is often employed

## 2.4. PHOTOELECTRON SPECTROSCOPY

for analysis of the band-structure of a solid material and work-function measurements. However, the electrons emitted from the core-levels of the atoms are used for analysis of a composition and a chemical state of a sample. In this study we employ the XPS in order to study a composition of the prepared molecular structures.

Surface sensitivity of the XPS is given by a mean-free-path (MFP) of the photoemited electrons in the studied material. The MFP is dependent on the kinetic energy of the electron. In general, the surface sensitivity of the XPS is in the range 1-10 nm.

The XPS measurement requires a monochromatic X-ray source. High demands are put on the X-ray sources, because a precisely defined energy of the photons is required in order to accurately determine an electron binding energy spectra of a sample. Sources emitting characteristic X-ray radiation are often used. We used an X-ray source equipped with aluminium and magnesium anodes for measurements performed within this thesis. The model of the used X-ray source is XR 50; it is commercially available from SPECS GmbH. Except the illumination source, the second important component of the XPS setup is the analyser of the kinetic energy of the emitted electrons.

The emitted electrons are collected, focused and accelerated by the electron optics into the entrance slit of the energy analyser. The hemispherical analyser is a common type of kinetic energy analyser used for the XPS measurements. The main parts of analyser are two concentric hemispherical electrodes. The electric field in the gap between the hemispheres allows to pass only the electrons with specific energy. In order to analyse a certain range of energies, the entrance energy of the electrons into the gap is swept and a number of passed electrons is recorded by a detector. The hemispherical analyser used within this thesis is Phobios 150 from SPECS GmbH. The XPS setup is mounted to the chamber connected to the UHV cluster (marked PES in Figure 2.1).

### 3. Self-assembly on graphene

In this chapter an experimental procedure together with a measurement analysis are presented. The subjects of the study are the self-assembled structures of a simple organic molecule on a graphene substrate and metal-organic network prepared on the graphene substrate. As an organic molecule suitable for supramolecular structure preparation we have chosen biphenyl-4,4-dicarboxylic acid (BDA). A structure of a building blocks plays an important role in the self-assembly process. Therefore, general characteristics of the BDA structure are described in Section 3.1.

The substrate used for graphene preparation within this study is Ir(111). The cleaning procedure of the Ir(111) substrate is presented in Section 3.2. Graphene grows epitaxially on Ir(111), therefore atomically clean substrate for the growths is required.

The growth and characterization of graphene on Ir(111) is discussed in Section 3.3. For the study of a self-assembly structure of the molecules a defect-free graphene is required. Imperfections in the substrate can induce defects in the supramolecular structure that grows on the substrate. Hence, the graphene suitable for preparation of the supramolecular structure is monocrystalline and it covers the whole surface of the substrate.

Section 3.4.1 is dedicated to the discussion related to preparation and study of the supramolecular structure of the BDA on graphene. For the study two different methods are used. The STM which allows to identify the structure of the system on the nanometer scale, but observation of large scale phenomena is not possible by STM. For the observation of the supramolecular structure on graphene in micrometer scale, the LEEM is used.

In the last section (3.5), a preparation of a metal-organic network is described, followed by the analysis of the metal-organic network by the temperature dependent XPS.

#### 3.1. Biphenyl-4,4-dicarboxylic acid

A model of the BDA molecule is shown in Figure 3.1. It is a relatively simple molecule comprising of two connected aromatic rings and two carboxyl groups on both ends. The aromatic rings ensure the flat adsorption on a substrate, as was observed on Cu(001) [57] and Au(111) [58] substrates.

The carboxyl groups are the main source of the intermolecular interactions in the BDA supramolecular structures. In the carboxyl group, an oxygen atom is bound to a hydrogen atom. Due to the high electron affinity of oxygen, the  $\sigma$ -bond between the hydrogen atom and the oxygen atom is highly polarized. Therefore, an electrostatic dipole is formed between the oxygen and the hydrogen atoms. A partial positive charge of the hydrogen atom in the carboxyl is strongly interacting with electron-rich parts of the molecule (red on el. potential map in Figure 3.1b and 3.1c). One of the electron-rich parts of the molecule is the second oxygen of the carboxyl group. The second oxygen is bound by one  $\sigma$ -bond and one  $\pi$ -bond to the neighbouring carbon atom. The carboxyl groups tend to form dimers, that are bound by the hydrogen bond [60, 61].

The deprotonation of the molecule significantly changes the intermolecular interaction. By deprotonation of the carboxyl group, a carboxylate ion is formed. In the carboxylate, two oxygen atoms bonded to the carbon atom are equivalent. The supramolecular structure of the deprotonated molecules is determined by a hydrogen bond, which is [57] formed

### 3.2. PREPARATION OF THE SUBSTRATE FOR GRAPHENE GROWTH

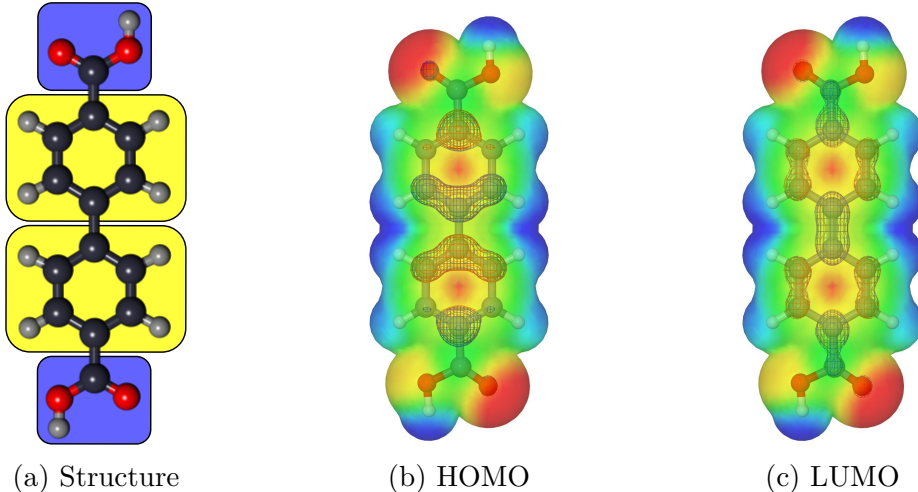


Figure 3.1: Structure of biphenyl-4,4-dicarboxylic acid (BDA). (a) An atomic structure model of BDA. The color code of the atoms in the model is following: carbon (black), hydrogen (gray) and oxygen (red). Different sub-structures are marked by the coloured background. The aromatic rings are marked by yellow color and the carboxyl groups are marked blue. (b) and (c) A calculated electrostatic potential of the molecule together with the shape of HOMO and LUMO, respectively. The orbitals are depicted by a wire-frame. All calculations of the molecular orbitals are performed on a molecule with planar geometry in MOPAC software by a semi-empirical method PM7 [59].

between the oxygen atom of the carboxylate ion and the hydrogen atoms bound to the aromatic ring. The deprotonation of the carboxyl group can be induced by adsorption on a reactive substrate or it can be induced by annealing.

## 3.2. Preparation of the substrate for graphene growth

The Ir(111) crystal surface is used for graphene preparation. Iridium is a convenient substrate for preparation of thin films and for the growth of epitaxial layers. The melting temperature of Ir is 2716 K [62]. The high melting temperature allows to thermally desorb most of the commonly used materials, therefore the cleaning process is facilitated. A common contaminant of iridium is carbon. Carbon can be removed from Ir by annealing in the oxygen atmosphere. During the annealing, carbon atoms migrate from the bulk of the crystal to the surface, where the atoms of carbon react with oxygen, forming CO and CO<sub>2</sub>. By this process, a carbon-depleted layer is formed at the surface of the crystal. During the annealing of Ir in oxygen atmosphere, the layer of Iridium oxides is formed on the surface. Therefore, after annealing in the oxygen atmosphere, flash-annealing at the temperature approx. 1400 K (decomposition temperature of IrO<sub>2</sub> [63]) is required in order to remove the surface oxide.

Removal of the segregated carbon by conventional Ar-ion sputtering is also possible. However, the annealing steps necessary to reconstruct the surface morphology after the sputtering has to be short approx. 30 s, otherwise carbon from the bulk migrates to the surface. The sputtering method was mostly used for the preparation of the clean Ir(111) surface.

### 3. SELF-ASSEMBLY ON GRAPHENE

All experiments within the thesis are performed with the Ir crystal supplied by MaTeck, GmbH. The hat-shaped crystal is mounted between two Mo plates which are screwed together by four M1.6 Mo bolts. The Mo sample plates allow manipulating with the crystal inside the UHV system.

The first cleaning step towards the crystal with an atomically clean surface, after insertion into the UHV system, is a degassing via an electron-beam heater. During the degassing the crystal is gradually heated to the temperature 700-900 K for the time >2 h. The long initial low-temperature annealing is necessary, in order to thermally desorb water and other molecules adsorbed under the ambient conditions. Furthermore, the degassing prevents the unnecessary desorption from the sample plate during the high-temperature annealing steps.

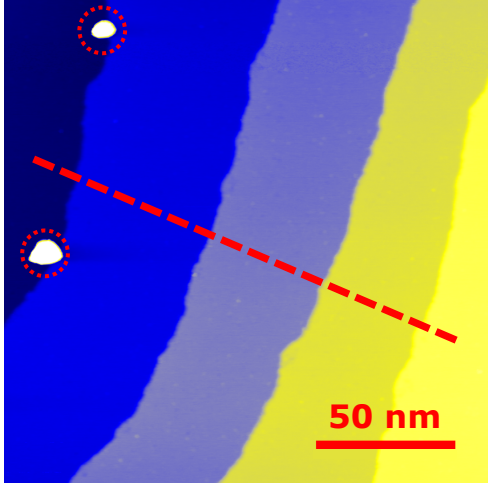
After the thorough degassing, the sample is cleaned by sputtering-annealing cycles, which begin with the sputtering step. Energy of the  $\text{Ar}^+$  ions is set in the range 1-2.5 keV. The direct influence of the sputtering energy on the resultant quality of the sample surface is not observed within this study. Duration of the initial sputtering step is set to 20 min, the following steps are 10-min-long. During the sputtering steps, the material from the topmost layers of the crystal is sputtered away. Therefore, the sputtering is a convenient technique for removal of the impurities which can not be thermally desorbed. Moreover, the surface structure of the crystal is highly disordered after the sputtering, hence, during the following annealing step, a new surface structure can be formed.

The annealing step plays a crucial role in the surface preparation process. The high-temperature annealing serves multiple purposes. It has to provide energy to the atoms of the crystal, high enough to allow migration of the surface atoms to thermodynamically stable positions. Furthermore, the Ar atoms incorporated into the crystal during the preceding sputtering step are desorbed from the crystal during the annealing. On the other hand, the surface atoms tend to react with the residual gas in the chamber, the pressure in the chamber has to be kept as low as possible. Therefore, the duration of the annealing step should be as short as possible and the low base pressure of the chamber is required. Last but not least, the temperature during the annealing has to be always lower than the melting temperature of the crystal, otherwise the defects in structure of the bulk crystal are introduced. The high melting temperature of Ir allows using short annealing steps with duration of 15-60 s at the temperatures 1400-1450 K. Multiple (3-10) sputtering-annealing cycles are necessary to prepare atomically clean surface. Parameters of the Ir cleaning process are summarized in Table 3.1.

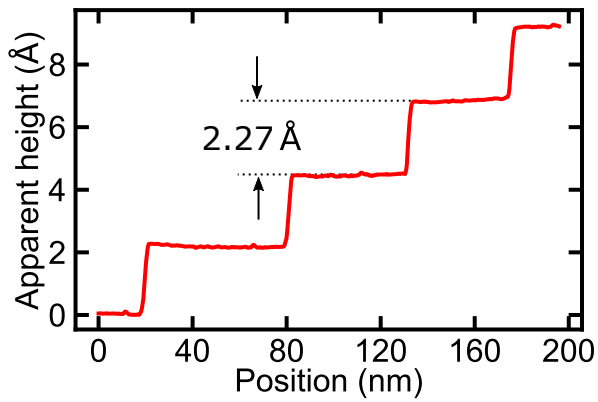
Table 3.1: The main parameters of the cleaning procedure. In the table Temperature ( $T$ ) and duration ( $t$ ) are stated. In the case of sputtering, the energy of the ions ( $E_i$ ) is added. The abbreviation "RT" is used for the room temperature.

Degassing	Sputtering	Annealing
$T=600\text{-}900 \text{ K}$	$T=\text{RT}$	$T=1400\text{-}1450$
$t>2 \text{ h}$	$t=10(20) \text{ min}$	$t=15\text{-}60 \text{ s}$
	$E_i=1\text{-}2.5 \text{ keV}$	

### 3.2. PREPARATION OF THE SUBSTRATE FOR GRAPHENE GROWTH



(a) STM overview image



(b) Line profile

Figure 3.2: STM analysis of the clean Ir(111) surface.(a) An overview STM scan on Ir(111) ( $U_b = -300$  mV;  $I_t = 300$  pA). Residual carbon impurities are marked by red dotted circles. (b) A line profile along the dashed line in (a). The measured apparent step height is labeled in the graph.

#### 3.2.1. STM analysis of Ir(111) surface

An STM image of the surface after the cleaning is shown in Figure 3.2a. Two spots in the dotted circles are residual carbon clusters. The carbon clusters are a result of an imperfect removal of carbon during the cleaning process. Nevertheless, a low concentration of the carbon impurities does not significantly affect the following graphene growth, nor formation of the terraces during the annealing steps.

The apparent height of the carbon impurities is in the range of 3-5 nm. In the STM topography images all the impurities appears to have the very same shape. The similarity in the shape of the carbon structures across the scan is an artifact of the STM measurement caused by a relatively high aspect ratio (the ratio of vertical and lateral dimension) of the carbon structures. The high aspect ratio of the probed structure leads to the fact that the constant current image in the vicinity of the structure reflects the shape of the tip. Therefore, this effect can be used as a method for characterization of the tip shape. The effect of the tip shape on the imaging properties of the scanning probe techniques is in details analyzed in reference [64]. Due to the described effect of the structures with high aspect ratio the real structure of carbon clusters cannot be resolved. Nevertheless, the preferential growth of the cluster attached to the step edges is frequently observed during the analysis of the cleaned Ir(111) surfaces.

The line-profile across several monoatomic steps is shown in Figure 3.2b. The width of the atomically clean terraces is in the range of 40-90 nm. The measured height of a monoatomic steps on the Ir(111) surface determined from five steps in the line-profile is  $(2.265 \pm 0.014)$  Å. The height  $h$  of the monoatomic step on the fcc(111) surface is related to the lattice parameter  $a$  by a simple relation  $h = a/\sqrt{3}$ . The lattice parameter of Ir measured by the x-ray diffraction is 3.831 Å [65]. Hence, the step height on the surface calculated from the lattice parameter is  $h = 2.212$  Å. A difference between the measured step height and the step height determined from the lattice parameter is probably caused by a miscalibration of the STM scanning unit.

### 3.3. Growth of epitaxial graphene

A growth of epitaxial graphene is the second step of the substrate preparation. The graphene is grown on the clean (111) surface of the Ir crystal. The growth procedure is performed in the LEEM setup. Therefore, *in-situ* observation of the graphene formation is possible. As the method of the graphene preparation, a combination of temperature programmed growth (TPG) and chemical vapor deposition (CVD) is chosen. The combined method of the graphene growth is necessary, in order to decrease the temperature required for the growth of graphene with single crystallographic orientation. The achievable process temperature in case of the preparation in the LEEM setup is limited by a design of the sample stage. According to the manufacturer, the maximum temperature which can be the sample stage exposed to is 1470 K. The sample is heated by an electron-beam heater that is build into the sample stage. The actual temperature is measured by a pyrometer attached to a view-port of the chamber. The ethylene gas is dosed into the chamber via a leak valve.

The first step in the used graphene growth procedure is an adsorption of the ethylene gas on the surface of the Ir crystal. The base pressure of the chamber is  $< 5 \cdot 10^{-10}$  mbar. In order to adsorb the ethylene gas on the sample surface, we exposed the crystal to an ethylene atmosphere. By regulation of the ethylene gas flow, the pressure in the chamber is set to the value  $1 \cdot 10^{-6}$  mbar. Therefore, most of the particles in the chamber are ethylene molecules. A saturation of the surface is required for the initial step of the graphene growth. Therefore, the time when the ethylene saturates the sample surface has to be estimated.

In the space filled with a gas at pressure  $p$  and temperature  $T$ , flux  $F$  of the gas particles through a unit area of space is given by an equation:

$$F = \frac{p}{\sqrt{2\pi mk_b T}}, \quad (3.1)$$

where  $m$  is the mass of the particles and  $k_b$  is the Boltzmann constant. This relation can be derived from the kinetic theory of gases. The sticking coefficient of the ethylene molecule on the Ir(111) surface is very close to unity [66]. Therefore, the flux of the molecules on unit area of the Ir(111) surface is equal to the deposition rate of the molecules on the surface. In saturation we assume that every surface atom of the Ir surface is covered by one molecule of ethylene. Areal density  $n$  of atoms on the Ir(111) surface can be calculated using a relation:

$$n = \frac{1}{a_{\text{Ir}}^2 \cos(60^\circ)}, \quad (3.2)$$

where  $a_{\text{Ir}} = 2.715 \text{ \AA}$  is length of the primitive lattice translation vector of the Ir(111) surface. Hence, the time  $\tau$  necessary to saturate the surface is determined by relation:

$$\tau = n/F. \quad (3.3)$$

If we assume the experimental conditions (summarized in table 3.2) during the adsorption of ethylene on the Ir(111) surface, the estimated time required for saturation by ethylene molecules is  $\tau = 9.44 \text{ s}$ . The presented estimation assume, independent sticking coefficient on the actual coverage of the substrate. In real experiment the sticking coefficient is decreeing with increasing coverage. Therefore, to be sure that the surface is saturated by

### 3.3. GROWTH OF EPITAXIAL GRAPHENE

Table 3.2: Summary of parameters required for the estimation of the adsorption time

Parameter	Value
$p$	$1 \cdot 10^{-6}$ mBar
$T$	300 K
$m$	28.05 u
$a_{\text{Ir}}$	2.715 Å

the ethylene molecules, the crystal is kept for longer than 1 min in the pressure  $10^{-6}$  mbar of ethylene during the adsorption step.

The second step of the graphene growth is the CVD of carbon on the substrate. The CVD is performed via annealing of the sample in the atmosphere of ethylene. During the initial annealing, the preadsorbed ethylene is decomposed and the residual carbon forms numerous islands of graphene attached to the step-edges of a (111) surface. The islands have a unique crystallographic orientation with respect to the Ir(111) substrate [67]. After the islands are formed, the area of the Ir surface that is not covered by graphene is exposed to the ethylene atmosphere. A new molecules of ethylene are adsorbed on the substrate. The newly adsorbed molecules dissociate because of the catalytic effect of the Ir surface and high temperature during the annealing. The residual carbon atoms after the decomposition of ethylene are attached to the already grown graphene islands maintaining the crystallographic orientation. Therefore, the grown layer of graphene has a unique orientation to the substrate. The whole process of the CVD needs to be slow in order to let the new carbon atoms settle in the most thermodynamically stable position maintaining the structure of the crystal. If the deposition of the new ethylene molecules is too fast, the growth process is limited by a kinetic factor and defects in the crystal occur. The most frequent defect is a different orientation of the graphene lattice with respect to the Ir substrate. Therefore, slow carbon deposition and high process temperature is the key to the preparation of high quality graphene.

The pressure of ethylene during the CVD step is set in range  $(1-5) \cdot 10^{-8}$  mbar. The process temperature of the crystal is set to 1370-1430 K. Duration of the CVD step is limited by the capabilities of the LEEM sample stage that starts to degas extensively after approximately 10 min at the process temperature. However, the complete coverage of the Ir surface by graphene is observed after the 8 min at the process parameters. The parameters of the graphene growth are listed in Table 3.3.

Table 3.3: Summary of the graphene growth parameters. The process temperature ( $T$ ), duration ( $t$ ) and pressure ( $p$ ) of the ethylene atmosphere are stated for both steps of the growth process.

Saturation	CVD
$T = RT$	$T = 1370 - 1430$ K
$t > 1$ min	$t = 8 - 10$ min
$p = 1 \cdot 10^{-6}$ mbar	$p = (1 - 5) \cdot 10^{-8}$ mbar

#### 3.3.1. STM analysis of graphene/Ir(111)

Overview STM micrograph of graphene grown over three Ir(111) terraces. In the image, the moiré pattern of graphene on Ir(111) surface is clearly resolved. The moiré pattern

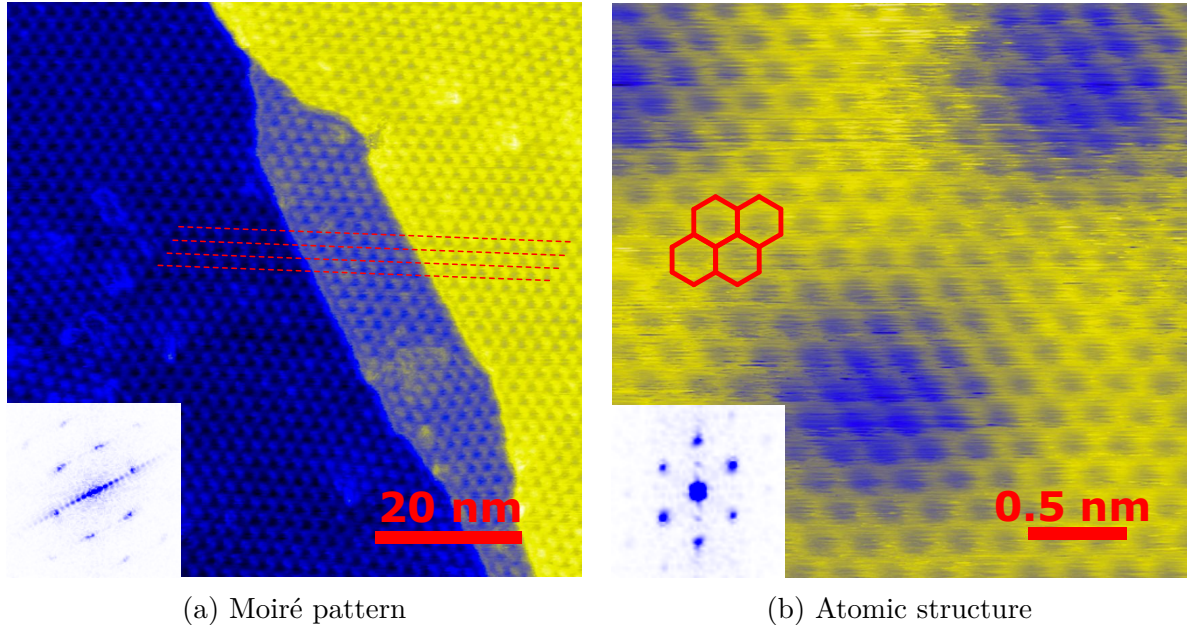


Figure 3.3: STM analysis of graphene (a) Overview STM image across two step-edges covered with graphene ( $U_b = 200$  mV;  $I_t = 200$  pA). The red dashed lines are guides for an eye aligned with the moiré pattern of graphene. The lowest spatial frequencies in a Fast Fourier Transform (FFT) spectra of the scan are shown in the inset. In the FFT, a pattern of the graphene moiré that exhibits a six-fold symmetry is clearly visible. A diagonal line across the spectra is the FFT of the step edges in the scan. The maximum spatial frequency displayed in the spectra is  $1\text{ nm}^{-1}$ . (b) STM micrograph of a graphene layer with atomic resolution ( $U_b = 30$  mV;  $I_t = 800$  pA). The red hexagons in the micrograph corresponds to the *honeycomb* lattice of graphene. A long-range variation of the contrast in the image corresponds to the moiré pattern. The lowest frequencies in the FFT of the micrograph are shown in the inset. The pattern in the FFT corresponds to the graphene lattice. The maximum spatial frequency displayed in the spectra is  $20\text{ nm}^{-1}$ .

is directly reflecting the orientation between the substrate and the graphene crystal. Due to the relatively large periodicity of the graphene moiré (approx. 2.5 nm), imaging of the moiré pattern is a convenient way how to reveal orientation of a graphene layer relative to the substrate. As long as the used substrate for graphene growth is single crystal, spatial variation of the moire pattern is always attributed to changes of the graphene layer crystallographic orientation. In the STM micrograph, the graphene grown across a three atomic traces is shown. It is worth to notice that the crystallographic orientation of graphene is very same on the both sides of the step-edges. The structural coherency of the graphene layer is proofed by the alignment of the moire patterns on both sides of the step-edges, as it is shown in the micrograph. The almost single crystalline character of the graphene layer is also revealed by the Fast Fourier Transformation (FFT) of the micrograph. In the FFT spectra, the pattern of the moiré lattice that exhibits a six-fold symmetry is pronounced. Furthermore, the FFT analysis revealed a small variation of the moire pattern across the image resulting in slightly blurred spots in the spectra.

The STM micrograph of graphene with atomic-scale resolution is presented in Figure 3.3b. In the image, a pronounced corrugation with a periodicity and symmetry of the graphene atomic lattice is shown. In order to demonstrate the correspondence of the

### 3.3. GROWTH OF EPITAXIAL GRAPHENE

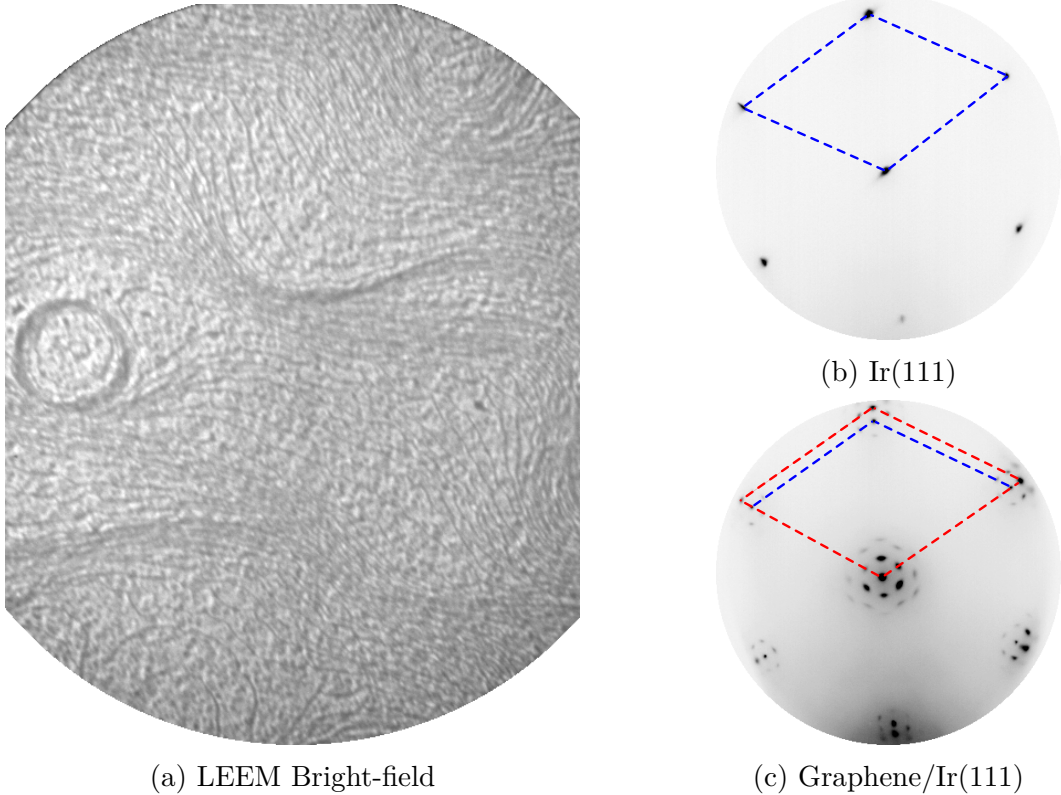


Figure 3.4: LEEM analysis of a grown graphene. (a) LEEM Bright-field micrograph ( $E_d = 2.98$  eV). View-field is  $5\text{ }\mu\text{m}$ . (b) LEED pattern of clean Ir(111). Blue rhombus depicts the primitive cell of Ir(111) in the reciprocal space (c) LEED pattern of graphene grown on the Ir(111) surface. The red rhombus shows the primitive cell of graphene crystal in the reciprocal space. Both diffraction patterns are obtained with energy of primary electrons 45 eV.

corrugation with the graphene lattice, a few periods of the *honeycomb* lattice is drawn in the image. Moreover, the pattern corresponding to the graphene lattice is also visible in the FFT spectra that is shown in the inset. A small elongation in a vertical direction of the hexagonal pattern in the FFT is probably caused by a distortion of the image by a drift during STM measurement.

### 3.3.2. LEEM analysis of graphene/Ir(111)

A micrograph of graphene grown on Ir(111) is shown in Figure 3.4a. The image is obtained by LEEM in the bright-field mode, hence a contrast in the image is related to the electron reflectivity of the surface. The LEEM in bright-field mode is convenient method for recognition of a graphene covered and a bare Ir surface. In the range of incident electron energy 2.5-5 eV, the reflectivity of the graphene is significantly higher than the reflectivity of the bare Ir(111) surface [67]. Therefore, the areas of bare Ir appears as a dark gray spots in the bright field image. The Ir surface shown in Figure 3.4a is not completely covered with graphene, the small dark areas on the edge of resolution can be seen in the image. Therefore, the image seems to be slightly speckled.

The atomic terraces in the image appears as a thin dark lines. Contrast on the step-edges in the bright-field mode arises from the interference of the electrons reflected on

### 3. SELF-ASSEMBLY ON GRAPHENE

both sides of the atomic-step [68]. Due to the interference contrast on a monoatomic steps two areas with relatively high density of steps are visible in the micrograph.

Structural quality of the prepared graphene can be probed by LEED. Figures 3.4b and 3.4c show LEED pattern of the clean Ir(111) surface and prepared graphene, respectively. The LEED pattern of the clean Ir(111) exhibit only sharp substrate spots corresponding to electron diffraction on (111) surface. The diffraction pattern of the graphene grown on Ir(111) is more complex. It consist substrate spots (marked by blue unit cell) and graphene (marked by red unit cell). The groups of satellite spots around each substrate and graphene spot, arise from diffraction on the moiré pattern. From the sharpness of the moiré spots is apparent that the graphene has unique orientation to the Ir(111) surface.

## 3.4. Structure of self-assembled BDA layers

In order to prepare BDA supramolecular structure, the thermal evaporation of the BDA on graphene substrate is performed. The BDA molecules are supplied by Sigma-Aldrich in form of a powder. The powder is placed in a crucible of oil-heated evaporation cell. Oil heated to the pre-set temperature circulates through a body of the cell and it heats the crucible. For the deposition of the molecules on the graphene substrate we used the sublimation temperature of the crucible 440 K. The sublimation temperature is the key factor affecting the deposition rate of the molecules on the substrate. For preparation of a clean molecular layers, the pressure during the evaporation has to be kept as low as possible.

The base pressure of the chamber where we deposit the molecules is  $< 5 \cdot 10^{-11}$  mbar. During the evaporation, the pressure in the chamber rise up to  $5 \cdot 10^{-10}$  mbar because of desorption from heated surfaces inside the chamber.

The first step in preparation of the self-assembled structure of the BDA is a thorough degassing of the evaporation cell and evaporated molecules. In order to remove all adsorbed gas on the surfaces of the evaporation cell, the cell is heated to the process temperature at least one hour before the deposition. The molecules in the crucible are evaporated into the chamber during the degassing. There is no harm caused by the evaporation of the molecules already during the degassing. Instead it is required, as the molecules on the surface of crucible filling are expose to all contaminants from the chamber for a long time.

The second step is the deposition of the molecules on the sample. We placed the substrate in front of the heated crucible in the cell, hence the molecules sublimated from the crucible adsorb on the sample surface. The sample is held at the room temperature during deposition. The precise rate of the deposition is not known. However from the depositions of BDA on Ag(001) performed in same configuration, it is roughly calibrated to 1 monolayer per 17 min. For study of the supramolecular structure of the BDA on the gaphene surface we use sub-monolayer coverages of molecules. In order to suppress the steric limitation of the supramolecular structure formation. Deposition times used for the preparation of the supramolecular system on graphene are in range 7-15 min. All parameters which we used for the deposition of the BDA are summarized in table 3.4.

### 3.4. STRUCTURE OF SELF-ASSEMBLED BDA LAYERS

Table 3.4: Summary of the BDA deposition parameters. The key parameters are cell temperature( $T$ ), duration ( $t$ ) and sample temperature ( $T_s$ ).

Degassing	Deposition
$T = 440\text{ K}$	$T = 440\text{ K}$
$t > 1\text{ h}$	$t = 7 - 15\text{ min}$
	$T_s = \text{RT}$

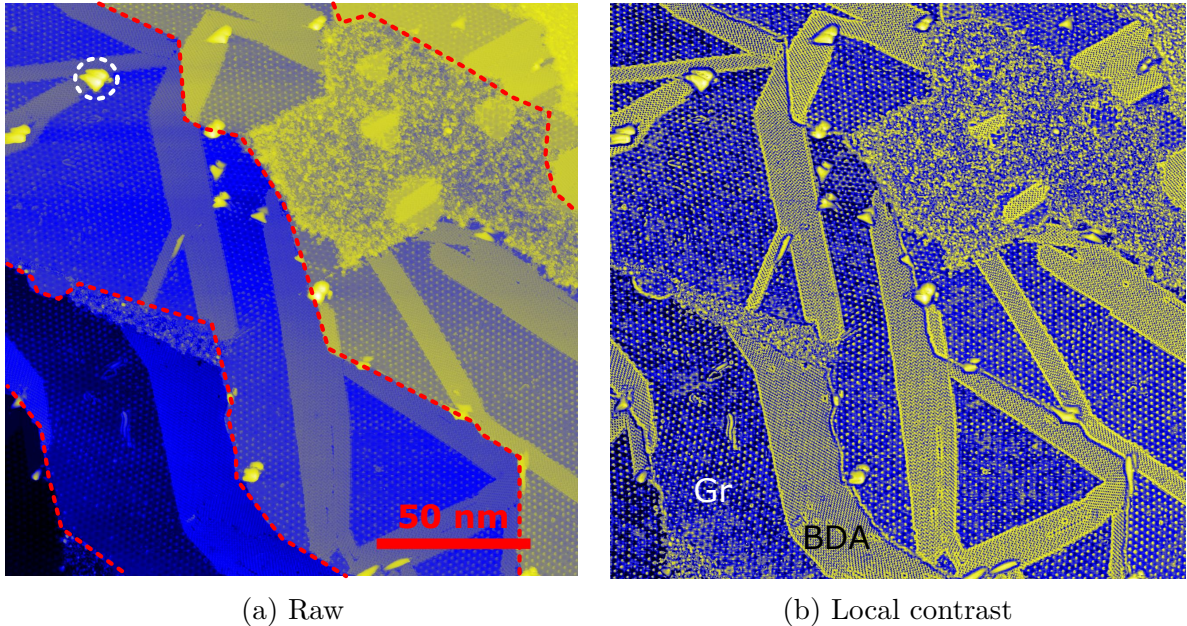


Figure 3.5: STM overview micrograph of molecular structure on graphene substrate. (a) STM overview of the sample after 7 min deposition of BDA ( $U_b = -300\text{ mV}$ ;  $I_t = 50\text{ pA}$ ). The red dashed lines indicate the monoatomic steps on the surface. (b) Local contrast modification of the micrograph (a). BDA molecules assembled into long stripes are pronounce on the flat graphene surface (labeled BDA). Graphene (labeled Gr) is recognized by the characteristic moiré pattern.

#### 3.4.1. STM study of BDA supramolecular structure

STM overview micrograph of a sample after 7 min deposition of BDA is presented in Figure 3.5a. In the micrograph, there are five atomic terraces separated by monoatomic steps. The step edges are slightly crooked that may be caused by low temperature during the Ir(111) substrate annealing. The small yellow features (an example is marked by white dashed circle in Figure 3.5a) in the micrograph are the carbon impurities segregated from the bulk Ir.

In order to show details of the micrograph, we employ a colour mapping technique based on the local contrast. The image coloured according to local contrast is shown in Figure 3.5b. In the micrograph is clearly visible a graphene moiré. Graphene covers almost whole area of the image. The unique orientation relative to the Ir(111) substrate can be determined from the unique orientation of the moiré.

The area in the top right corner exhibits strong disorder. Nature of this disordered structure is not fully understand. The possible explanation is a too high temperature, during graphene growth. Due to high growth temperature, the carbon atoms are dissolved

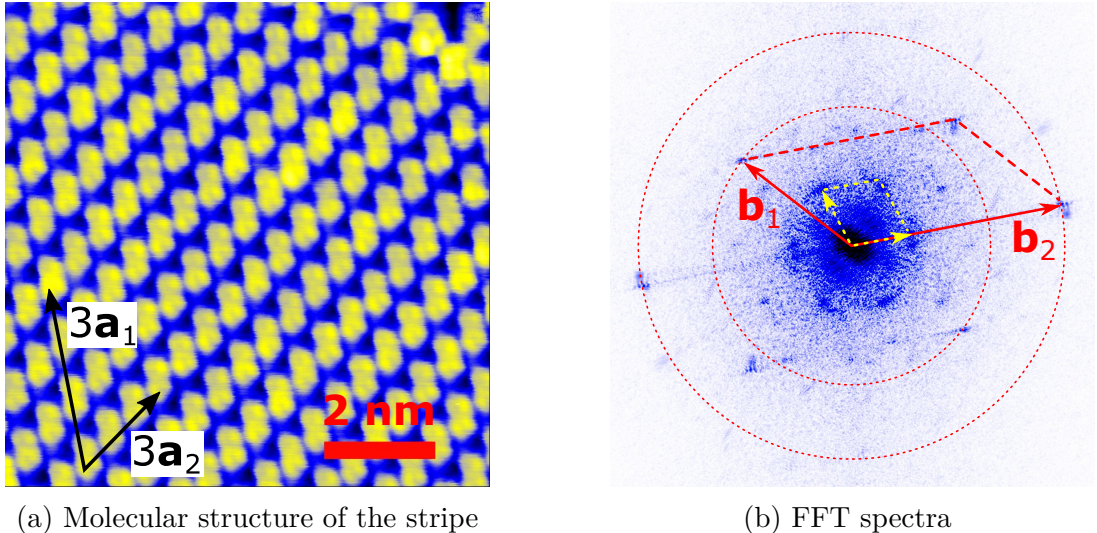


Figure 3.6: Molecular superstructure of BDA on graphene. (a) STM detailed micrograph of the molecular structure ( $U_b = -300$  mV;  $I_t = 55$  pA). The image is a detail of a stripe domain in Figure 3.5a. Lengths of the primitive lattice vectors labelled in the image are  $a_1 = 13.7$  Å and  $a_2 = 8.1$  Å. (b) FFT spectrum of the overview image shown in Figure 3.5a. Reciprocal lattice vectors corresponding to the lattice in (a) are labeled by red colour; those of graphene moiré are yellow. The dashed circles serve as guide for an eye to identify a different rotation domains. Maximum displayed spatial frequency in the spectra is  $2 \text{ nm}^{-1}$  ( $k = 1/\lambda$ ).

in bulk of the Ir crystal. Dissolved carbon atoms segregate on the surface during cooling and they form a disordered carbon layer. This behaviour was observed on a Rh(111) surface by Dong et al. [69]. However, the carbon solubility in Ir is roughly four times lower than in Rh [70]. Hence, the observation of this phenomena during graphene growth on Ir requires higher temperature to reach a significant concentration of the carbon atoms in Ir bulk. A further investigation of the disordered structure formation is needed in order to improve a quality of prepared graphene. In any case, disordered structure on the surface does not affect the formation of the molecular structure on the surface of graphene.

The BDA molecules on a graphene substrate are arranged into a stripe domains. The domains are stable at room temperature during STM imaging. However, we do not observe single molecules adsorbed on the graphene. This is caused by the high mobility of the BDA molecules on the graphene substrate at room temperature.

The stripe domains tends to grow in straight lines preferentially aligned along the Ir step-edges. Preferential nucleation of the molecular structures on the step-edges is an frequently observed behaviour in molecular systems where the diffusivity of the molecules over the surface is high. It can be explained by a stronger dispersive interaction of the molecule with a substrate, when the molecule is placed next to the step-edge compared to molecule adsorbed on the flat terrace. Therefore, the adsorption sites next to the step-edge are preferred.

A detailed STM scan of a stripe domain is shown in Figure 3.6a. The BDA molecules appears in the scan as an elongated protrusions with a slightly corrugated surface. The scan reveal a periodic structure within the stripe domain. The lattice in which the molecules are ordered can be described by two primitive lattice vectors enclosing angle

### 3.4. STRUCTURE OF SELF-ASSEMBLED BDA LAYERS

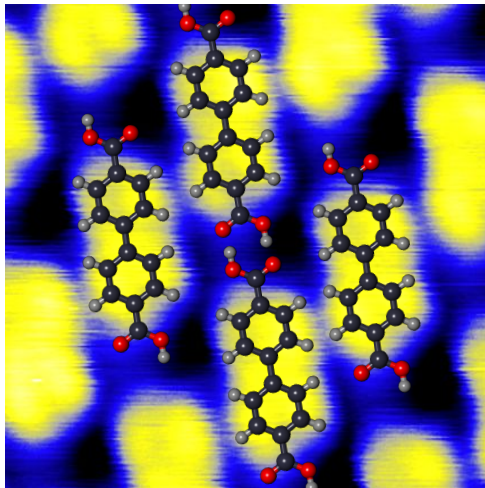


Figure 3.7: High-resolution STM micrograph of BDA supramolecular structure ( $U_b = -300$  mV;  $I_t = 50$  pA). Models of the BDA molecules are drawn inside the scan in order to demonstrate actual orientation of the molecules in the structure. The distance between the oxygen atoms of two carboxyl groups within a BDA molecule is 11.4 Å.

approx. 55°. The lattice vectors are drawn in the image. Vector  $\mathbf{a}_1$  is always pointing parallel to the direction of the stripe domain. The second lattice vector is preferentially oriented parallel to the lattice vector of the moiré pattern as can be seen in the FFT spectra which is presented in Figure 3.6b.

Hexagonal pattern of graphene moiré is pronounced in the FFT. The reciprocal lattice vectors of the moiré are drawn in the FFT by yellow colour. Reciprocal unit cell of the lattice presented in Figure 3.6a is also clearly visible in the FFT spectra. Therefore, the preferential orientation of the supramolecular structure relative to the graphene lattice is visible. The existence of the preferential orientation is a clear sign of a graphene moiré interaction with a molecules within the structure.

Nevertheless, rotational domains of the molecular lattice are also visible in the FFT. The observation of rotational domains is possible due to a weak molecule-substrate interaction overpowered by different effect. One of the possible effects is the effect of the step-edges, which provide nucleation centres for a new domains. Step-edges together with impurities restricts a diffusion of the molecules across the surface, therefore a nucleation of a new rotated stripe domain often takes place nearby. In order to fully understand the structure of the BDA on the graphene substrate, the interactions between individual molecules has to be analysed.

The high resolution STM image is presented in Figure 3.7. The hydrogen bonds are the main molecule-molecule interaction within the BDA supramolecular structure. The BDA molecules are bound together by a complementary hydrogen bonds between the carboxyl group.

The directionality of the hydrogen bond together with prolonged shape of the molecule ensures formation of the strong hydrogen bonded chains. This chains are propagating along the  $\mathbf{a}_1$  translation vector of the molecular structure. Along the lattice vector  $\mathbf{a}_2$ , the chains interact much weaker. Iteration between the chains is taking place between the oxygen atom of the carboxyl group and a hydrogen atom bound to the aromatic ring. Due to weak interaction between the molecular chains, a defects in alignment of the chain are frequently observed.

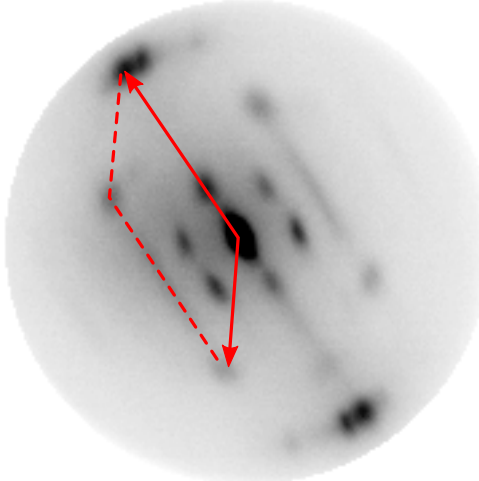


Figure 3.8: LEED pattern of the sample analysed by STM in previous section. Energy of the primary electron is 7 eV. Red arrows label a reciprocal unit cell of the BDA superstructure. Diameter of the primary beam is roughly 20  $\mu\text{m}$ .

A difference in the intensity of the molecule-molecule interaction in the two directions explains many aspects of the observed structure. The straight stripe domains grow because of the high stability of linear structures stabilized by the relatively strong hydrogen bond. The edges of the stripe domains are straight without defects, because an extraction of the molecule from the side of the domain requires high energy necessary to break two pairs of hydrogen bonds; it is not a favourable process. On the other hand, formation of hydrogen bonded chain is very favourable process, hence no free ends of the chains are observed. The hydrogen bond is in nature electro-static interaction, therefore it can act on a relatively large distances (2.5 Å–3.5 Å) compared to the covalent bond or the dispersive interaction. Hence, the hydrogen bond allows to propagate the supramolecular structure over the step-edges of Ir(111). This effect can be found in the upper part of the micrograph in Figure 3.5b, where the stripe domain is grown over a step-edge.

In order to study the BDA structure on a large scale, we employ a LEEM technique. The goal of the LEEM study is to extend the description of the molecular structure beyond the scanning range of the STM.

### 3.4.2. LEEM study of BDA supramolecular structure

For the direct comparison of the structure of the BDA on the graphene substrate, we perform LEED experiment. The observed LEED pattern is shown in Figure 3.8. The pattern is qualitatively very similar to the FFT of the STM overview micrograph presented in Figure 3.6b. The diffraction pattern has to be calibrated according to a well-known structure to obtain the values of the lattice parameters from the diffraction pattern. We use a periodicity of the graphene moire 25.4 Å as a reference.

The lattice parameters calculated from the LEED pattern are 11.2 Å and 7.2 Å. A discrepancy between the period of the lattice determined by analysis of the FFT spectrum of the STM image and by analysis of the LEED pattern may be caused by several factors. Nevertheless, we often observe underestimation of the period deduced from LEED patterns. Hence, the lattice parameters are probably underestimated as the calculated lattice parameter 11.2 Å is smaller than the length of the molecule (11.4 Å in a gas phase).

### 3.5. IRON-COORDINATED BDA NETWORK

Furthermore, we observed a strong influence of the electron beam on the supramolecular structure. The electrons apparently destroy a long-range order of the supramolecular structure. Hence, the diffraction pattern fades out no the time scale of seconds during observation of the LEED. However, the effect is much more pronounced at higher energy (10-40 eV) of the primary electrons.

## 3.5. Iron-coordinated BDA network

In order to prepare a metal coordinated molecular structure, we deposit the BDA molecules and iron atoms on the graphene surface. The iron is a suitable coordination centre for a design of the metal-organic networks. Use of iron atoms as coordination centers in combination with the BDA ligands have been demonstrated on a Cu(100) [71]. The formation of the coordination bond between a carboxylic acid and an iron atom requires the deprotonation of the carboxyl group. The molecules of the BDA are spontaneously deprotonated upon deposition on the reactive Cu(100) substrate. On the contrary, the BDA persists in the protonated form upon deposition on graphene substrate as we demonstrate in the previous section. The deprotonation occurs on the graphene substrate after annealing of the mixture of the iron atom and BDA molecules on the graphene surface.

A key factor for the formation of the metal-organic network with a long-range order is a correct concentration of the coordination centers and ligands in the mixture deposited on the surface. The second factor affecting the structure of the resultant assembly is the temperature of the substrate during deposition or during annealing performed after deposition. Demonstration of both factors, concentration, and temperature, on the structure of the iron coordinated dicarboxylic acid on the Cu(100) substrate can be found in reference [72]. Elevated temperatures are necessary to overcome the diffusion barrier of the molecules on the substrate and facilitate the deprotonation of the carboxylic groups.

For the preparation of the metal-organic structures, we employ multiple combinations of the deposition of the BDA and iron. The BDA deposition on the graphene substrate is performed in the very same manner as in preparations described in the previous section. Iron is deposited on the graphene substrate from an electron-beam evaporator. Deposition rates of iron on the graphene substrate are in range  $0.4\text{--}2.6 \text{ ML/h}$  ( $1 \text{ ML} = 2.71 \cdot 10^{15} \text{ cm}^{-2}$  is a number of Ir surface atoms per unit area). In order to estimate a suitable iron coverage for a complete monolayer of the Fe coordinated BDA structure, we assume the same binding motif as was observed on the Cu(100) [71]. The areal density of Fe atoms in the coordinated structure on Cu(100) is approx.  $7.7 \cdot 10^{13} \text{ cm}^{-2}$ .

In the first step of the study of the iron-coordinated molecular structure, we investigate the deprotonation process of the BDA by a method of the temperature dependent XPS. As long as the BDA molecules persist in the protonated form on the graphene surface, the deprotonation has to occur during the process of metal-coordinated structure formation. The process of deprotonation cause change of binding environment of oxygen atom in the carboxyl group of the BDA. Therefore, the binding energy of electrons at the core-levels of the oxygen changes. The changes of the binding energy during the deprotonation can be detected as the change of an oxygen photoemission line shape. Furthermore, a formation of a coordination bond changes the binding environment of an iron atom. Therefore, a photoemission line shape of the iron atom is also changing as a result of the metal-organic network building process.

### 3. SELF-ASSEMBLY ON GRAPHENE

We also performed a LEEM study of the metal-organic structure formed on the graphene substrate. Molecule-molecule interaction in the metal-coordinated BDA structure is mainly the coordination bond of the molecules around the iron center. This interaction is completely different compared with hydrogen bond in the BDA self-assembled structure. As long as the molecule-molecule interaction is one of the key aspects affecting the supramolecular structure formation, we expect a structural transformation as a result of the formation of the coordination bonds between the molecules. In order to observe this structural transformation, we deposited the BDA molecules and the iron atoms on the substrate at room temperature and transfer the sample to the LEEM apparatus. Observation of the sample during annealing reveal a structural transformation of the molecules on the surface.

The STM study of the metal-organic structure on the graphene surface cannot be performed due to unavailability of the STM during the time of the experiments aimed at the metal-organic network.

#### 3.5.1. Temperature dependent XPS study of Fe-BDA structure

In order to probe the deprotonation of the BDA molecules, we codeposit molecules and iron atoms on the graphene substrate at room temperature. The crystal is transferred into a stage of the XPS setup after deposition. The stage is equipped with a built-in electron-beam heater. A filament of the electron beam heater that is placed close to the back side of the crystal is used for the heating of the sample by heat radiation. Heating the crystal by radiation heating is advantageous for slow and precise control of the temperature in range 300-500 K. The temperature of the crystal is monitored via K-type thermocouple mounted in contact with the molybdenum plate which holds the crystal in the stage. The temperature of the sample is increased step-wise during measurement by increasing the current driven through the filament. The spectra are obtained always after temperature stabilization.

The crystal is illuminated by X-ray generated by a source. An aluminum anode is used, so the energy of the illuminating photons is 1486.6 eV, corresponding to the  $K\alpha$  line in the emission spectra of Al. Normal orientation of the sample surface to the analyser is set in the experiment. The presented photoemission spectra are average spectra after roughly 1 hour acquisition in the case of Fe and O and 20 min in the case of Ir. Long accumulation times are required to obtain sufficient signal to noise ratio.

Even though the long accumulation times are used, the amount of the iron atoms, required for the formation of one monolayer of the metal-coordinated network, is far below detection limit of our XPS setup. Therefore, samples prepared for the XPS analysis were prepared with high coverage of the molecules and the Fe atoms. High coverage of the substrate with the mixture of the components is required to obtain the reasonable intensity of the photoemission lines of oxygen and iron mainly.

Because of high coverage, the formation of the long-range ordered structures is sterically restricted. However, proper mixing of two components is ensured by the codeposition. The codeposition of the BDA molecules and iron atoms is performed for 30 min. The evaporation temperature of the molecules during the codeposition is set to 438 K. The amount of deposited molecules is roughly equivalent to 1.7 monolayers of the self-assembled structure on Ag(100) substrate. Nevertheless, sticking coefficient of the molecules on the graphene substrate is probably lower than sticking coefficient on Ag(100).

### 3.5. IRON-COORDINATED BDA NETWORK

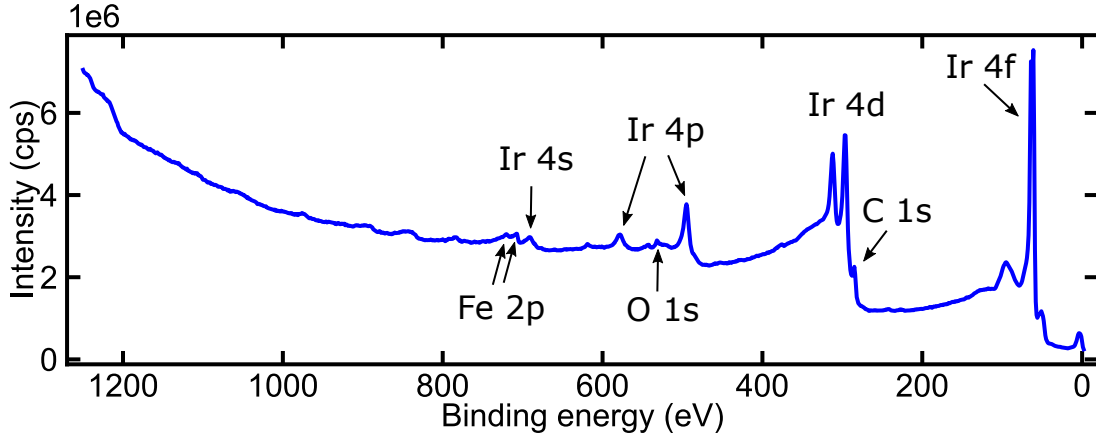


Figure 3.9: Overview photoemission spectra of the sample after deposition at room temperature. The main photoemission lines are labelled.

Iron atoms are codeposited simultaneously with the BDA molecules for the full 30 min. The deposition rate of Fe is calibrated via the QCM measurements. The deposition rate used for the deposition of Fe is 0.8 ML/h. Therefore, the amount of the iron deposited on the surface corresponds to approx. 13.5 monolayers of the metal-coordinated BDA structure. Iron, that is not bound in the coordinated structure tends to form clusters on the graphene surface, therefore a fingerprint of metallic iron is expected in the XPS spectra measured on the prepared sample.

In order to roughly identify the composition of the sample, we measure an overview spectra. The overview is presented in Figure 3.9. The most pronounced peaks in the spectra correspond to the Ir substrate. The weak lines in the spectra can be attributed to the Fe, O, and C deposited on the surface.

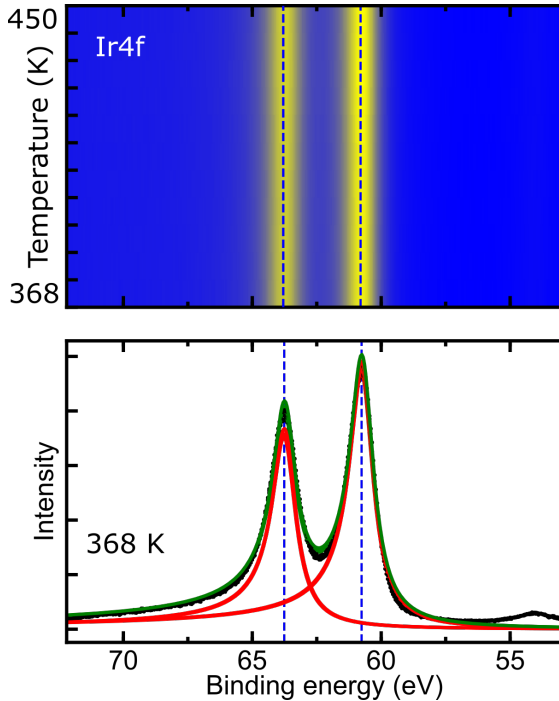
The most widely used spectral feature used for the analysis of the deprotonation of organic molecules is a carbon photoemission line. However, the analysis of the carbon emission line is very limited in the case of organic molecules deposited on the graphene on Ir, as the C1s peak is overshadowed by the intensive Ir4d substrate peaks. Therefore, we use high-resolution spectra of the O 1s peak and Fe 2p doublet for the analysis of the process. Spectra of the Ir 4f are measured as a reference to determine any effect of charging during the long experiment.

The measured spectra of the Ir 4f doublet are shown in Figure 3.10a. In the top 2D plot is shown the dependency of the measured intensity on the binding energy (x-axis) and the temperature (y-axis) measured on the sample. In the bottom graph, a typical spectrum of Ir 4f doublet observed at 368 K is presented.

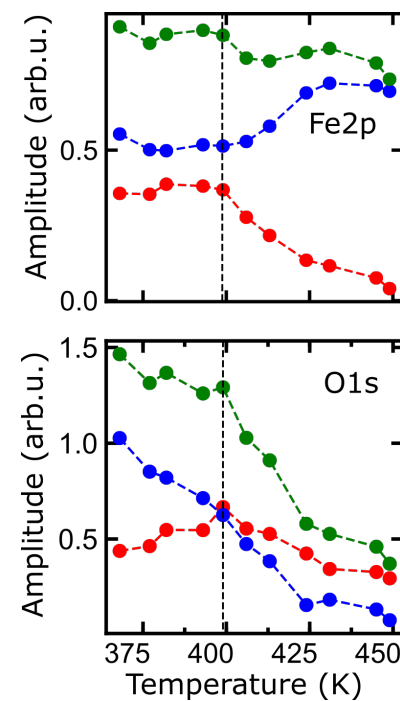
The peak position of the two peaks in the spectra is determined by fitting of the spectra. Two asymmetric Doniach-Sunjic line profiles [73] together with Tougaard background [74] are used to fit the spectra. The found position of the two peaks (60.7 eV and 63.7) is in agreement with previous observation on Ir(111) [66].

The positions of the Ir 4f peaks is independent on the sample temperature. This can be seen in the 2D plot in 3.10a, where the doublet appears as two bright bands parallel to the temperature axis. When the binding environment of the Ir atoms is changed during the heating the photoemission peak shifts or deforms. The shift or deformation of the peak would result in the modulation of the bands along the temperature axis. The modulation is not present in the 2D plot of Ir 4f doublet. Therefore, the changes in the

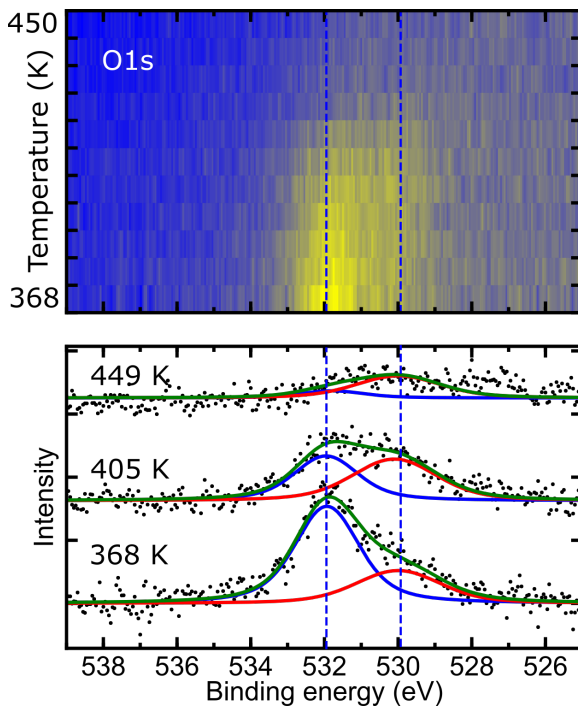
### 3. SELF-ASSEMBLY ON GRAPHENE



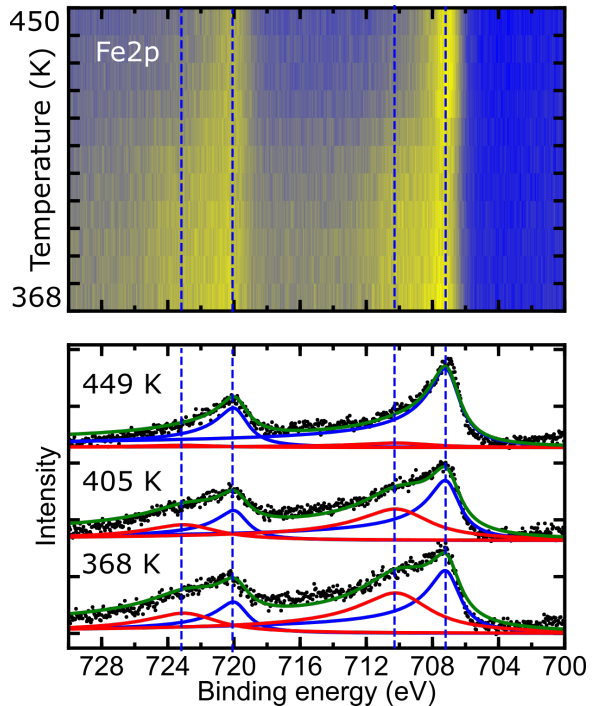
(a) Ir 4f



(b) Temperature dependency of the components



(c) O 1s



(d) Fe 2p

Figure 3.10: Temperature dependent XPS study of Fe-BDA interaction on a graphene substrate. 2D plots display dependency of a measured intensity on the binding energy and temperature. Vertical dashed lines label the energy position of the peaks in the XPS spectra below each 2D plot. (a) shows a temperature dependency of the Ir 4f doublet in 2D plot along with a spectrum measured at the sample temperature 368 K. (c) and (d) show a temperature dependency of O 1s and Fe 2p peaks. Dependency of the fitted peak amplitudes on the temperature is shown in (b). Red and blue colours correspond to the line colour of the peaks and green labels are sum of the two amplitudes.

### 3.5. IRON-COORDINATED BDA NETWORK

binding environment of the Ir atoms are not observed in the temperature range 368 K–450 K. However, making conclusion related to the reaction on the surface is not possible, as long as the majority of the Ir 4f signal originates from the bulk crystal.

Changes of O 1s peak during annealing is clearly visible in the 2D plot in Figure 3.10c. The O 1s peak is initially pronounced at the binding energy of 532 eV and with temperature it shifts towards lower binding energies and at approx. 400 K it starts to loose the intensity. This behaviour can be described on the basis of the detailed analysis of the peak line shape.

The model used for the description of the spectra consists of a linear background and two Voight-profiles. The peaks are centered at the binding energies 532 eV and 530.1 eV. The initial values of the parameters are adjusted during the fit of the spectra which is measured at the sample temperature 368 K. After fitting of the first spectra the position and width parameters are fixed. During the fitting of the spectra measured at a higher temperature, the only amplitude of the peaks is adjusted. By this procedure, the model gain stability necessary for the fitting of spectra measured at higher temperatures. The high stability of the model is crucial for the fitting of the data with relatively low signal to noise ratio.

The peak centred at the binding energy 532 eV can be associated to an partially deprotonated BDA molecules. The partially deprotonated terephthalic acid molecules on the Cu(100) surface show a pronounced peak centred at 531.7 eV [75]. The binding environment of the oxygen is also affected by the hydrogen bond between carboxylic groups and charge transfer, which may results in the peak shifts.

The peak centred at the binding energy 532 eV can be associated to partially deprotonated BDA molecules. The partially deprotonated terephthalic acid molecules on the Cu(100) surface show pronounce peak centred at 531.7 eV [75]. The binding environment of the oxygen is also affected by the hydrogen bond between carboxylic groups and charge transfer, which may result in the peak shifts.

The second peak centred at lower binding energies (530.1 eV) can be associated with the oxygen bound to the metal atom [76]. Therefore, it can be associated with the binding between carboxylate and an iron atom.

The optimized amplitudes of the two peaks are presented in the bottom plot in Figure 3.10b. In the graph can be distinguished two temperature regions, where the amplitudes of the peaks show different trends. The transition between the regions is at approx. 400 K. The growth of the amplitude of the component located at 530.1 eV is obvious (red dots). The growth can be interpreted as increasing number of molecules bound to the Fe atom. At 400 K the trend of the curve change suddenly and both components starts to losing an intensity. This behavior can be explained by reaching the evaporation temperature of the BDA from the graphene surface. As long as, the only known source of oxygen on the surface originates from the carboxylic groups of the BDA, evaporation of the molecules from the surface is a natural explanation of the observation.

As the bond between the carboxylic group and Fe atom is formed, the binding environment of the Fe atom changes. Therefore, a change in the photoemission peak of Fe should be observed. The detail spectra of Fe 2p peak is presented in Figure 3.10d. The temperature dependency of the peak shape is visible in the top 2D plot. The initially broad asymmetric peaks are losing the asymmetry with increasing temperature. This is a clear sign of the change of the Fe atoms binding environment. For the quantitative analysis of the change of the peak, we employ a model consisting of four asymmetric

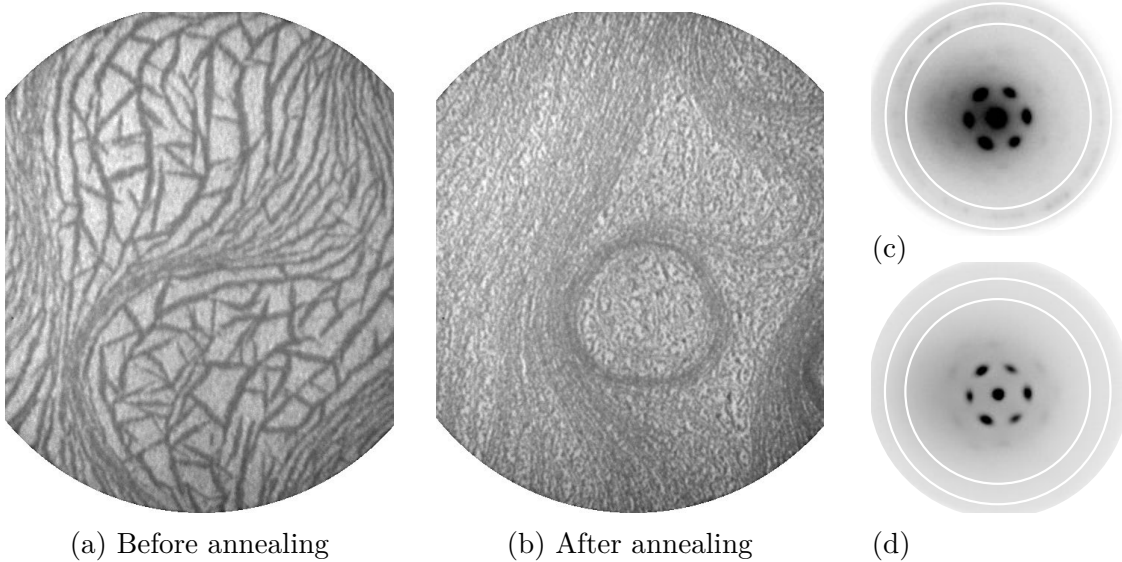


Figure 3.11: LEEM analysis of Fe-BDA system. (a) and (b) are LEEM bright-field micrographs ( $E_d = 4.5$  eV) of the sample before annealing and after annealing at approx. 380 K. View-field is 3  $\mu\text{m}$ . (c) and (d) LEED pattern of the sample before annealing and after the annealing. Energy of the primary beam is 8 eV and 8.9 eV, respectively. White circles border the area of spatial frequencies corresponding to the self-assembled structure of the BDA on graphene. This measurement was performed by Ing. Lukáš Kormoš.

Doniach-Sunjic line profiles and a Tougaard background. Both peaks of doublet are fitted simultaneously. One pair of the peaks represents a metallic state of the iron (blue line), whereas the oxygen bounded state is represented by the second pair (red line). The position of the Fe 2p<sub>3/2</sub> peak of the metallic state is determined as 707 eV, which is in agreement with usually observed value as well as the position of the Fe 2p<sub>1/2</sub> peak at 719.8 eV [77]. The second pair of peaks can be associated with higher oxidation states of the Fe atoms Fe<sup>2+</sup> and Fe<sup>3+</sup>. The peak positions of the second pair of peaks are 709.9 eV and 722.7 eV.

Evolution of the amplitudes of the Fe 2p peaks is presented in a top plot in Figure 3.10b. As in the case of O 1s peak, the two temperature regions can be distinguished with respect to the amplitude of the higher oxidation states peak (red markers). The amplitude of the peak is constant up to the temperature 400 K, when it starts to decrease. This is in correlation with the behaviour of the peak centred at 530 eV in a spectrum of O 1s peak, which starts to disappear at the very same temperature.

From the temperature dependent behaviour of the peaks, we can estimate the evaporation temperature of the molecules from the surface as 400 K. Moreover, the common aspects of the temperature dependency of peaks of Fe and O peaks may be interpreted as a formation of a bond between the BDA molecules and Fe atoms on the surface at the temperature below 400 K. However, to prove this explanation, we need to perform STM analysis of the samples after codeposition of the BDA molecules and Fe in order to reveal a molecular structure.

### 3.5. IRON-COORDINATED BDA NETWORK

#### 3.5.2. LEEM study of Fe-BDA structure

In the previous section, we observed a temperature dependent changes of binding environments of oxygen and iron atoms. In order to observe the potential formation of the metal-organic network on the surface, we codeposit the BDA molecules together with Fe atoms on the graphene substrate at room temperature. For the LEEM study, we employ lower coverages of the molecules and iron compared with samples prepared for the XPS study. Sub-monolayer coverages are required to remove a steric limitation during a potential formation of the metal-coordinated network. Deposition of the BDA is performed for 15 min. The evaporation parameters of the BDA molecules are set the same as in the previous deposition experiments.

The deposition of iron is performed in two intervals during the BDA deposition. The intervals are 1 min and 1.5 min long. The first deposition of iron is performed 9 min and the second 13 min after the beginning of the BDA deposition. Two short intervals are used in order to operate the iron evaporator with high flux to ensure the stable deposition rate. The amount of the deposited iron is roughly corresponding to the number of coordination centres in 1 ML of Fe-BDA network. The estimation of the required amount of Fe is based on the observation of the Fe-BDA coordinated network on Cu(100) substrate [71].

The sample is transferred into the LEEM chamber after deposition. The LEEM micrograph of the prepared sample is shown in Figure 3.11a. Dark areas in the image correspond to graphene covered by domains of the self-assembled molecules. As can be seen, the domains are preferentially attached to the step edges of the Ir(111) surface. This is in agreement with STM observation presented in Section 3.4.1. In the LEED pattern shown in the Figure 3.11c, we can identify the spatial frequencies corresponding to the self-assembled structure of the BDA on the surface. Even though the spots are barely visible, multiple rotational domains can be resolved in the pattern. Both LEEM and LEED observations are in agreement with a previous study of the BDA molecules self-assembled on the graphene surface [78]. Therefore, the effect of the Fe atoms codeposited with the BDA molecules is not apparent.

After analysis of the sample structure, we anneal the sample at approx. 380 K for 10 min. The annealing step is performed in order to facilitate the reaction between carboxylic groups and Fe atoms on the surface and increase a mobility of the deposits on the surface.

The LEEM bright-field image of the sample after annealing is presented in Figure 3.11b. The sample is cooled to the room temperature. Small patches of dark grey colour are distributed evenly over the sample surface. These dark areas can be associated with molecules adsorbed around a binding site in form of the metal cluster on the surface. The observed structure is in sharp contrast with the structure observed before annealing. Therefore, a different molecule-molecule interaction or a molecule-substrate interaction have to play a role.

The LEED pattern of the sample after annealing is shown in Figure 3.11d. Graphene moiré spots are the only present in the pattern. Therefore, the structure of the molecules on the surface does not exhibit long-range order that could give a rise to diffraction spots in the image.

This could be explained by binding of the molecules to a Fe cluster formed on the graphene substrate. If the molecules are not able to remove single atoms from the clusters, the molecules will stay connected to the cluster and does not participate on the supramolecular structure formation. This scenario would explain the observation of a disordered

### *3. SELF-ASSEMBLY ON GRAPHENE*

structure on the surface after annealing as well as the reactions observed by the temperature dependent XPS measurement. The second possible explanation is an incorrect ratio between a number of molecules and Fe atoms deposited on the surface, which could restrict the formation of the ordered structure. The STM analysis would reveal the true configuration of the molecules on the surface, as it does not require long-range order to resolve the molecular structure.

## 4. Conclusion

This thesis is focused on the self-assembly properties of a carboxylic acid on a graphene substrate. The studied system is biphenyl-4,4-dicarboxylic acid deposited on graphene grown on the Ir(111) substrate. The preparation and the analysis process was performed within a UHV system. The sample was analysed by three different techniques: STM, LEEM and XPS.

First, we prepared the clean Ir(111) substrate by the standard combination of sputtering and annealing cycles. The morphology of the prepared surface was analysed by the STM, which revealed atomically flat terraces of the width of tens of nanometres. On the cleaned substrate, we prepared graphene from an ethylene precursor by a combination of the chemical vapour deposition and the temperature programmed growth methods. The growth of the graphene in the LEEM setup allowed a direct observation of the process. The morphology of the graphene layer was probed by LEEM and STM techniques. The large crystalline grains with single orientation relative to the Ir(111) substrate and an almost full coverage of the surface were observed. Such a high-quality graphene layer is required for the growth of the supramolecular structures.

We deposited organic molecules on the graphene substrate by thermal evaporation. An oil-heated effusion cell was employed in order to achieve the stable evaporation temperature of 438 K. The sample was kept at room temperature during the deposition. Nevertheless, the weak interaction of the molecules with the substrate ensures a mobility of the molecules on the surface high enough to form self-assembled structures with long-range order.

The ordered structure of the molecules on the surface was observed during LEED experiments which also revealed an instability of the molecular structure upon an electron-beam irradiation. We performed a thorough study of the self-assembled structure by the STM technique. The observed binding motif is based on hydrogen bonding of the carboxylic groups in straight molecular chains. The chains on the surface are bound together in the stripe domains aligned preferentially along the substrate step-edges. Moreover, the preferential alignment of the molecules with respect to the densely-packed directions of the graphene moiré was observed both in LEED and in STM experiments.

In the second part of the thesis, we made first steps towards building the metal-organic network on the graphene surface. As graphene offers the unique charge and spin transport properties, it is an interesting substrate for an investigation of the substrate-mediated interactions between coordinated metallic centres. We focussed on the preparation of the system comprised the Fe coordination centres linked by the BDA molecules. We probed the on-surface reaction of Fe and carboxylic groups by a method of the temperature dependent XPS. Furthermore, the effect of the on-surface reaction on the molecular structure was observed by LEEM.

The Fe atoms were deposited on the graphene substrate at room temperature together with the BDA molecules, to prepare a suitable mixture of potential coordination centres and organic ligands. The temperature dependent XPS study revealed an increasing number of carboxylic groups bound to Fe atoms in the temperature region of 368-400 K as well as the critical temperature 400 K when the BDA molecules start to evaporate from the graphene surface. At temperature 450 K the molecules are completely removed from the surface. This observation was taken into account during the following experiments focused on the analysis of the metal-organic network structure by the LEEM.

#### 4. CONCLUSION

To prepare the Fe coordinated BDA structure, we codeposited sub-monolayer coverages of the BDA molecules and the Fe atoms on the graphene substrate at room temperature. A LEEM analysis of the sample revealed a self-assembled structure of the molecules without any effect of the codeposited Fe atoms. However, after annealing of the sample at the temperature of 380 K, the structure changed significantly. Molecules previously assembled into the stripe domains mostly growing along a step-edges on the surface were observed in small clusters distributed evenly over the sample surface. Nevertheless, we did not observe any long-range order that could be ascribed to the metal-organic network. Two explanations of the observation are possible, either the composition of the mixture of Fe atoms and BDA molecules was not suitable or the deposited Fe atoms formed clusters on the graphene substrate. In both cases, the STM study would reveal the structure, however, the STM was not available during the presented experiment.

In near future, we would like to study the process of the metal-organic structure formation in the Fe-BDA system by the methods of STM and optimize the process to prepare highly ordered metal-organic structures on the graphene substrate.



# References

- [1] Whitesides, G. M. and Grzybowski, B. Self-assembly at all scales. *Science*, 295(5564): 2418–2421, 2002.
- [2] Stepanow, S., Lin, N. and Barth, J. V. Modular assembly of low-dimensional coordination architectures on metal surfaces. *Journal of Physics: Condensed Matter*, 20(18):184002, 2008.
- [3] Girovsky, J., Nowakowski, J., Ali, M. E. et al. Long-range ferrimagnetic order in a two-dimensional supramolecular Kondo lattice. *Nature Communications*, 8:15388, 2017.
- [4] Kalf, F., Rebergen, M. P., Fahrenfort, E. et al. A kilobyte rewritable atomic memory. *Nature Nanotechnology*, 11(11):926–929, 2016.
- [5] Graham, M. J., Zadrozny, J. M., Fataftah, M. S. et al. Forging Solid-State Qubit Design Principles in a Molecular Furnace. *Chemistry of Materials*, 29(5):1885–1897, 2017.
- [6] Khajetoorians, A. A., Wiebe, J., Chilian, B. et al. Realizing all-spin-based logic operations atom by atom. *Science*, 332(6033):1062–1064, 2011.
- [7] Li, J.-R., Sculley, J. and Zhou, H.-C. Metal–organic frameworks for separations. *Chemical Reviews*, 112(2):869–932, 2011.
- [8] Horcajada, P., Chalati, T., Serre, C. et al. Porous metal–organic-framework nanoscale carriers as a potential platform for drug delivery and imaging. *Nature Materials*, 9 (2):172, 2010.
- [9] Gutzler, R., Cardenas, L. and Rosei, F. Kinetics and thermodynamics in surface-confined molecular self-assembly. *Chemical Science*, 2(12):2290–2300, 2011.
- [10] Barth, J. V., Costantini, G. and Kern, K. Engineering atomic and molecular nanostructures at surfaces. *Nature*, 437(7059):671, 2005.
- [11] London, F. The general theory of molecular forces. *Transactions of the Faraday Society*, 33:8b–26, 1937.
- [12] Gao, H.-Y., Wagner, H., Held, P. A. et al. In-plane Van der Waals interactions of molecular self-assembly monolayer. *Applied Physics Letters*, 106(8):081606, 2015.
- [13] Hunter, C. A. and Sanders, J. K. The nature of  $\pi$ - $\pi$  interactions. *Journal of the American Chemical Society*, 112(14):5525–5534, 1990.
- [14] Bersuker, I. B. *Electronic structure and properties of transition metal compounds: introduction to the theory*. John Wiley & Sons, 2010.
- [15] Gambardella, P., Stepanow, S., Dmitriev, A. et al. Supramolecular control of the magnetic anisotropy in two-dimensional high-spin Fe arrays at a metal interface. *Nature Materials*, 8(3):189, 2009.

## REFERENCES

- [16] Sun, J. T., Lu, Y. H., Chen, W. et al. Linear tuning of charge carriers in graphene by organic molecules and charge-transfer complexes. *Physical Review B*, 81:155403, 2010.
- [17] Otero, R., de Parga, A. V. and Gallego, J. Electronic, structural and chemical effects of charge-transfer at organic/inorganic interfaces. *Surface Science Reports*, 72(3):105–145, 2017.
- [18] Wallace, P. R. The band theory of graphite. *Physical Review*, 71(9):622, 1947.
- [19] Novoselov, K. S., Geim, A. K., Morozov, S. V. et al. Electric field effect in atomically thin carbon films. *Science*, 306(5696):666–669, 2004.
- [20] Miao, F., Wijeratne, S., Zhang, Y. et al. Phase-coherent transport in graphene quantum billiards. *Science*, 317(5844):1530–1533, 2007.
- [21] Katsnelson, M., Novoselov, K. and Geim, A. Chiral tunnelling and the Klein paradox in graphene. *Nature Physics*, 2(9):620, 2006.
- [22] Cooper, D. R., D’Anjou, B., Ghattamaneni, N. et al. Experimental review of graphene. *ISRN Condensed Matter Physics*, 2012:1–56, 2012.
- [23] Dean, C. R., Young, A. F., Meric, I. et al. Boron nitride substrates for high-quality graphene electronics. *Nature Nanotechnology*, 5(10):722, 2010.
- [24] Bolotin, K. I., Sikes, K., Jiang, Z. et al. Ultrahigh electron mobility in suspended graphene. *Solid State Communications*, 146(9-10):351–355, 2008.
- [25] Emtsev, K. V., Bostwick, A., Horn, K. et al. Towards wafer-size graphene layers by atmospheric pressure graphitization of silicon carbide. *Nature Materials*, 8(3):203, 2009.
- [26] Li, X., Magnuson, C. W., Venugopal, A. et al. Graphene films with large domain size by a two-step chemical vapor deposition process. *Nano Letters*, 10(11):4328–4334, 2010.
- [27] Jung, I., Pelton, M., Piner, R. et al. Simple approach for high-contrast optical imaging and characterization of graphene-based sheets. *Nano Letters*, 7(12):3569–3575, 2007.
- [28] Martin, J., Akerman, N., Ulbricht, G. et al. Observation of electron–hole puddles in graphene using a scanning single-electron transistor. *Nature Physics*, 4(2):144, 2008.
- [29] Järvinen, P., Hääläinen, S. K., Banerjee, K. et al. Molecular self-assembly on graphene on SiO<sub>2</sub> and h-BN substrates. *Nano Letters*, 13(7):3199–3204, 2013.
- [30] Choucair, M., Thordarson, P. and Stride, J. A. Gram-scale production of graphene based on solvothermal synthesis and sonication. *Nature Nanotechnology*, 4(1):30, 2009.
- [31] Bhuyan, M. S. A., Uddin, M. N., Islam, M. M. et al. Synthesis of graphene. *International Nano Letters*, 6(2):65–83, 2016.

## REFERENCES

- [32] Li, Z., Wu, P., Wang, C. et al. Low-temperature growth of graphene by chemical vapor deposition using solid and liquid carbon sources. *ACS Nano*, 5(4):3385–3390, 2011.
- [33] An, H., Lee, W.-J. and Jung, J. Graphene synthesis on Fe foil using thermal CVD. *Current Applied Physics*, 11(4):S81–S85, 2011.
- [34] Roth, S., Osterwalder, J. and Greber, T. Synthesis of epitaxial graphene on rhodium from 3-pantanone. *Surface Science*, 605(9-10):L17–L19, 2011.
- [35] Li, X., Cai, W., An, J. et al. Large-area synthesis of high-quality and uniform graphene films on copper foils. *Science*, 324(5932):1312–1314, 2009.
- [36] Kim, K. S., Zhao, Y., Jang, H. et al. Large-scale pattern growth of graphene films for stretchable transparent electrodes. *Nature*, 457(7230):706, 2009.
- [37] Coraux, J., Engler, M., Busse, C. et al. Growth of graphene on Ir(111). *New Journal of Physics*, 11(2):023006, 2009.
- [38] López, G. and Mittemeijer, E. The solubility of C in solid Cu. *Scripta Materialia*, 51(1):1–5, 2004.
- [39] Bhaviripudi, S., Jia, X., Dresselhaus, M. S. et al. Role of kinetic factors in chemical vapor deposition synthesis of uniform large area graphene using copper catalyst. *Nano Letters*, 10(10):4128–4133, 2010.
- [40] Chan, C.-C., Chung, W.-L. and Woon, W.-Y. Nucleation and growth kinetics of multi-layered graphene on copper substrate. *Carbon*, 135:118–124, 2018.
- [41] Seah, C.-M., Chai, S.-P. and Mohamed, A. R. Mechanisms of graphene growth by chemical vapour deposition on transition metals. *Carbon*, 70:1–21, 2014.
- [42] Pletikosić, I., Kralj, M., Pervan, P. et al. Dirac cones and minigaps for graphene on Ir(111). *Physical Review Letters*, 102(5):056808, 2009.
- [43] Coraux, J., Plasa, T. N., Busse, C. et al. Structure of epitaxial graphene on Ir(111). *New Journal of Physics*, 10(4):043033, 2008.
- [44] Lu, J., Yeo, P. S. E., Zheng, Y. et al. Using the graphene moiré pattern for the trapping of C<sub>60</sub> and homoepitaxy of graphene. *ACS Nano*, 6(1):944–950, 2011.
- [45] Hattab, H., N'Diaye, A., Wall, D. et al. Growth temperature dependent graphene alignment on Ir(111). *Applied Physics Letters*, 98(14):141903, 2011.
- [46] van Gastel, R., N'Diaye, A., Wall, D. et al. Selecting a single orientation for millimeter sized graphene sheets. *Applied Physics Letters*, 95(12):121901, 2009.
- [47] Riss, A., Wickenburg, S., Tan, L. Z. et al. Imaging and tuning molecular levels at the surface of a gated graphene device. *ACS Nano*, 8(6):5395–5401, 2014.
- [48] Cai, Y., Zhang, H., Song, J. et al. Adsorption properties of CoPc molecule on epitaxial graphene/Ru(0001). *Applied Surface Science*, 327:517–522, 2015.

## REFERENCES

- [49] Hamalainen, S. K., Stepanova, M., Drost, R. et al. Self-assembly of cobalt-phthalocyanine molecules on epitaxial graphene on Ir(111). *The Journal of Physical Chemistry C*, 116(38):20433–20437, 2012.
- [50] Zhou, H., Zhang, L., Mao, J. et al. Template-directed assembly of pentacene molecules on epitaxial graphene on Ru(0001). *Nano Research*, 6(2):131–137, 2013.
- [51] Binnig, G., Rohrer, H., Gerber, C. et al. Surface studies by scanning tunneling microscopy. *Physical Review Letters*, 49(1):57, 1982.
- [52] Lægsgaard, E., Besenbacher, F., Mortensen, K. et al. A fully automated, ‘thimble-size’ scanning tunnelling microscope. *Journal of Microscopy*, 152(3):663–669, 1988.
- [53] Lægsgaard, E., Österlund, L., Thostrup, P. et al. A high-pressure scanning tunneling microscope. *Review of Scientific Instruments*, 72(9):3537–3542, 2001.
- [54] Chen, J. C. *Introduction to Scanning Tunneling Microscopy*. Oxford University Press, 2008.
- [55] Tromp, R., Mankos, M., Reuter, M. et al. A new low energy electron microscope. *Surface Review and Letters*, 5(06):1189–1197, 1998.
- [56] Bauer, E. *Surface microscopy with low energy electrons*, volume 23. Springer, 2014.
- [57] Stepanow, S., Lin, N., Vidal, F. et al. Programming supramolecular assembly and chirality in two-dimensional dicarboxylate networks on a Cu(100) surface. *Nano Letters*, 5(5):901–904, 2005.
- [58] Zhu, N., Osada, T. and Komeda, T. Supramolecular assembly of biphenyl dicarboxylic acid on Au(111). *Surface Science*, 601(8):1789–1794, 2007.
- [59] Stewart, J. J. Optimization of parameters for semiempirical methods VI: more modifications to the NDDO approximations and re-optimization of parameters. *Journal of Molecular Modeling*, 19(1):1–32, 2013.
- [60] Canas-Ventura, M., Klappenberger, F., Clair, S. et al. Coexistence of one-and two-dimensional supramolecular assemblies of terephthalic acid on Pd(111) due to self-limiting deprotonation. *The Journal of chemical physics*, 125(18):184710, 2006.
- [61] Clair, S., Pons, S., Seitsonen, A. P. et al. STM study of terephthalic acid self-assembly on Au(111): Hydrogen-bonded sheets on an inhomogeneous substrate. *The Journal of Physical Chemistry B*, 108(38):14585–14590, 2004.
- [62] Hunt, L. A history of iridium. *Platinum Metals Review*, 31(1):32–41, 1987.
- [63] Chaston, J. Reactions of oxygen with the platinum metals. *Platinum Metals Review*, 9(2):51–56, 1965.
- [64] Meyer, E., Hug, H. J. and Bennewitz, R. *Scanning probe microscopy: the lab on a tip*. Springer Science & Business Media, 2013.

- [65] Owen, E. and Yates, E. XLI. Precision measurements of crystal parameters. *The London, Edinburgh, and Dublin Philosophical Magazine and Journal of Science*, 15 (98):472–488, 1933.
- [66] Marinova, T. S. and Kostov, K. Adsorption of acetylene and ethylene on a clean Ir(111) surface. *Surface Science*, 181(3):573–585, 1987.
- [67] Loginova, E., Nie, S., Thürmer, K. et al. Defects of graphene on Ir(111): Rotational domains and ridges. *Physical Review B*, 80(8):085430, 2009.
- [68] Chung, W. and Altman, M. Step contrast in low energy electron microscopy. *Ultra-microscopy*, 74(4):237–246, 1998.
- [69] Dong, G., van Baarle, D. W., Rost, M. et al. Graphene formation on metal surfaces investigated by in-situ scanning tunneling microscopy. *New Journal of Physics*, 14 (5):053033, 2012.
- [70] Arnoult, W. J. and McLellan, R. B. Solubility of carbon in rhodium, ruthenium, iridium and rhenium. Technical report, William Marsh Rice Univ., Houston, Tex., 1972.
- [71] Stepanow, S., Lin, N., Barth, J. V. et al. Surface-template assembly of two-dimensional metal- organic coordination networks. *The Journal of Physical Chemistry B*, 110(46):23472–23477, 2006.
- [72] Lingenfelder, M. A., Spillmann, H., Dmitriev, A. et al. Towards surface-supported supramolecular architectures: tailored coordination assembly of 1, 4-benzenedicarboxylate and Fe on Cu(100). *Chemistry-A European Journal*, 10 (8):1913–1919, 2004.
- [73] Doniach, S. and Sunjic, M. Many-electron singularity in X-ray photoemission and X-ray line spectra from metals. *Journal of Physics C: Solid State Physics*, 3(2):285, 1970.
- [74] Tougaard, S. Universality classes of inelastic electron scattering cross-sections. *Surface and Interface Analysis*, 25(3):137–154, 1997.
- [75] Fuhr, J. D., Carrera, A., Murillo-Quirós, N. et al. Interplay between hydrogen bonding and molecule–substrate interactions in the case of terephthalic acid molecules on Cu(001) surfaces. *The Journal of Physical Chemistry C*, 117(3):1287–1296, 2013.
- [76] Shen, L.-h., Bao, J.-f., Wang, D. et al. One-step synthesis of monodisperse, water-soluble ultra-small  $\text{Fe}_3\text{O}_4$  nanoparticles for potential bio-application. *Nanoscale*, 5 (5):2133–2141, 2013.
- [77] Lozzi, L., Passacantando, M., Picozzi, P. et al. Oxidation of the  $\text{FeCu}(100)$  interface. *Surface Science*, 331:703–709, 1995.
- [78] Khokhar, F. S., van Gastel, R. and Poelsema, B. Role of topographical defects in organic film growth of 4, 4-biphenyldicarboxylic acid on graphene: A low-energy electron microscopy study. *Physical Review B*, 82(20):205409, 2010.

# List of abbreviations

BDA	biphenyl-4,4-dicarboxylic acid
CoPc	cobalt phthalocyanine
CVB	1,3,5-Tris-(2,2-dicyanovinyl)benzene
CVD	chemical vapor deposition
DC	deposition chamber
fcc	face-centered-cubic
FFT	fast Fourier transform
Gr	graphene
hBN	hexagonal boron nitride
HOMO	highest occupied molecular orbital
LEED	low energy electron diffraction
LEEM	low energy electron microscopy
LUMO	lowest unoccupied molecular orbital
MCP	micro channel plate
MFP	mean-free-path
MOF	metal-organic framework
PC	preparation chamber
PEEM	photo emission electron microscopy
PES	photo-electron spectroscopy
QCM	quartz crystal microbalance
STM	scanning tunneling microscopy
TPG	temperature programed growth
TS	transfer system
UPS	ultra-violet photoelectron spectroscopy
UHV	ultra high vacuum
XPS	X-ray photoelecton spectroscopy